ANATOMICAL LANDMARK BASED REGISTRATION of CONTRAST ENHANCED-T1 WEIGHTED MAGNETIC RESONANCE IMAGES

by

Ali Demir

Submitted to the Graduate School of Engineering and Natural Sciences
in partial fulfillment of
the requirements for the degree of
Master of Science

Sabancı University
Spring 2010

Anatomical Landmark Based Registration of Contrast Enhanced-T1 Weighted Magnetic Resonance Images

APPROVED BY

Assist. Prof. Dr. Gözde ÜNAL .....
(Thesis Supervisor)

Prof. Dr. Aytül ERÇİL .....

Assoc. Prof. Dr. Mustafa ÜNEL .....

Assist. Prof. Dr. Müjdat ÇETİN .....

Assist. Prof. Dr. Selim Balcısoy .....

DATE OF APPROVAL: .....

to my family

Acknowledgements

I would like to express my gratitude to my thesis supervisor Gözde Ünal for her support and encouragement throughout my thesis. This work can not be completed without her help and great motivation. I also would like to thank to our clinical partner Anadolu Medical Center and our team member Dr. Kutlay Karaman for his valuable guidance and support.

I would like to thank Mr. Yousef Jameel for providing financial support for my graduate education.

My valuable thanks go to all my colleagues at Vision and Pattern Analysis Laboratory, for their great friendship.

I owe special thanks to Gözde Gül İşgüder, Mehmet Umut Şen, Demet Yılmaz, and Süheyla Çetin for standing by me in both good and bad times.

Finally, I would like to thank my father Hüseyin Demir, my mother Hanım Demir, and my brothers Musa and Mustafa Demir for their endless support throughout my life. Their great love made everything possible.

ANATOMICAL LANDMARK BASED REGISTRATION of CONTRAST ENHANCED-T1 WEIGHTED MAGNETIC RESONANCE IMAGES

Ali Demir

EE, M.Sc. Thesis, 2010

Thesis Supervisor: Gözde ÜNAL

Keywords: registration, medical image registration, follow-up change detection in serial MRI, contrast enhanced T1-weighted magnetic resonance images

Abstract

In many problems involving multiple image analysis, an image registration step is required. One such problem appears in brain tumor imaging, where baseline and follow-up image volumes from a tumor patient are often to-be compared. Nature of the registration for a change detection problem in brain tumor growth analysis is mainly rigid. Contrast enhanced T1-weighted MR images (CE-T1 MRI) are widely used in clinical practice for monitoring brain tumors. Over this modality, contours of the active tumor cells and whole tumor borders and margins are visually enhanced. In this thesis, a new technique to register serial CE-T1 MRI is presented. The proposed fully-automated method is based on five anatomical landmarks: eye balls, nose, confluence of sagittal sinus, and apex of superior sagittal sinus. After extraction of anatomical landmarks from fixed and moving volumes, a rigid transformation is estimated by minimizing the sum of squared distances between the landmark coordinates. Final result is refined with a surface registration, which is based on head masks confined to the surface of the scalp, as well as to a plane constructed from three of the extracted features. The overall registration is not intensity based, and it depends only on the inherent anatomical structures. Validation studies using both synthetically transformed MRI data, and real MRI scans, which included several markers over the head of the patient were performed.

In addition, comparison studies against manual landmarks marked by a radiologist, as well as against the results obtained from ITK mean squares and cross correlation based methods were carried out to demonstrate the effectiveness of the proposed method.

KONTRASTLI-T1 MAGNETİK REZONANS GÖRÜNTÜLERİNİN ANATOMİK REFERANS NOKTASI TABANLI ÇAKIŞTIRILMASI

ALİ DEMİR

EE, Yüksek Lisans Tezi, 2010

Tez Danışmanı: Gözde ÜNAL

Anahtar Kelimeler: çakıştırma, medikal görüntülerin çakıştırılması, MR takip görüntülerinde değişim analizi, kontrastlı-T1 MR görüntüsü

Özet

Birden fazla görüntünün incelenmesini gerektiren analizlerde görüntülerin çakıştırılması işlemi sıklıkla kullanılır. Beyin tümörü görüntülemede ilk çekilen görüntü ile takip görüntülerinin karşılaştırılması, bu görüntülerin çakıştırılması ile gerçekleştirilebilir. Beyin tümörünün zamana baglı degişimi problemindeki çakıştırma işleminin temel yapısı geregi katı dönüşüm tabanlı çakıştırma yapılır. Rutin beyin tümörü incelemelerinde kontrastlı-T1 magnetik rezonans (MR) görüntüleri her zaman kullanılır. Bu görüntülerde tümörün dış çeperi genellikle kontrast tutar ve parlak olarak görülür. Bu tez çalışmasında kontrastlı-T1 MR görüntülerinin çakıştırılması için bir yöntem önerilmiştir. Önerdigimiz yöntemde otomatik olarak 5 farklı anatomik yapı (burun, sag ve sol göz yuvarlaklari, torkular herofili, superior sagital sinüs tepe noktası) bölütlenir ve bu yapıların üzerinde anatomik referans noktaları belirlenir. Referans ve takip görüntüleri üzerinde hesaplanan referans noktaları kullanılarak katı dönüşüm tabanlı çakıştırma işlemi gerçekleştirilir. Bu aşamada referans noktaları arasındaki farkı en aza indiren katı dönüşüm parametreleri en küçük kareler (least squares) yöntemi ile hesaplanabilir. Elde edilen çakıştırılmış görüntü, daha hassas bir sonuç elde etmek için, ikincil bir yöntem ile düzeltilir. Bu yöntemde ilk yöntemden elde edilen görüntüden ve referans görüntüsünden çıkartılan kafa yüzeyleri 3 referans noktası ile sınırlandırılarak kullanılmıştır.

Önerdigimiz bu çakıştırma yöntemi voksel şiddetine baglı degildir ve sadece zamana baglı degişim göstermeyecek anatomik yapılara baglıdır. Algoritma sınama çalışmaları sentetik dönüşüm parametleri kullanılarak oluşturulan gerçek görüntüler ve MR takip görüntüleri üzerinde yapılarak algoritmanın performansı degerlendirilmiştir. Ayrıca takımımızdaki radyolog doktor kontrolünde manuel referans noktaları işaretlenerek yapılan çakıştırma yöntemi ile karşılaştırılmıştır. Önerilen yöntem kütüphanelerine kolayca ulaşılabilen voksel şiddeti tabanlı çakıştırma yöntemleri (ITK) ile de karşılaştırılarak sonuçlar belirtilmiştir.

Table of Contents

List of Figures

List of Tables

Chapter 1

Introduction

1.1 Literature Review and Motivation

Image registration refers to the problem of finding a geometric transformation, which is optimal in a certain sense, between two or more corresponding images. Nature of the correspondence problem describes the type of necessary geometric transformation [1]. Registration is a major problem in many medical imaging applications such as image guided neurosurgery, surgical planning, radiotherapy planning, patient population analysis, and monitoring tumor growth.

In this thesis, we focused on the registration of serial Magnetic Resonance (MR) images intended for the change detection problem in tumor monitoring [5, 6]. General methods and strategies for image registration are reviewed in [2, 3], and [4]. Registration problem for change detection in brain can be classified as a rigid body motion of invariant brain structures. The most challenging part of the change detection is to overlay invariant structures accurately. In [8], Intracranial cavity (ICC) is used as an invariant structure to register serial images through computation of dense point correspondences based on segmented ICC. Anatomical landmark localization on Talairach atlas and initial atlas based segmentation are also popular approaches for registration [15, 18, 16, 17]. In [9], the outer cortical surface and major sulcal ribbons were extracted to register brain MR images. Geometrical features such as curves, lines, curvatures, corners, and so on, are also used extensively in image registration problems. Davatzikos et. al. use the curves and boundaries in regions to preregister the volumes for elastic registration [10, 11]. Klein et al. evaluated available volume based and surface based brain image registration techniques [12]. Geometric landmarks make the registration procedure automatic and robust

[13, 14, 19]. On the other hand, intensity similarity based methods [20, 21, 22] are also widely utilized in most of the registration problems. In the review paper [5], Duffau et al. reported that the image intensity is not a reliable measure in the presence of growing tumors, which introduce additional challenges for registration algorithms. Therefore, detection of invariant landmarks in serial images is expected to perform better than an intensity similarity based optimization approach.

Registration is inherently an ill-posed problem, therefore usually no unique solution is available. Often, constraints are introduced. Particularly for a deformable registration problem, constraints on a deformation field can be defined. On the other hand, depending on the domain and application of the problem, specific intensity similarity measures or different feature-based approaches are proposed [1]. For the clinical problem of brain tumor monitoring, where anatomical features can be extracted from the CE-T1 MRI, this thesis presents a new method where strong anatomical features drive the registration without depending on intensity similarity measures, which can become problematic in presence of significant tumor change over time [5]. Another advantage of the proposed approach is that it is invariant due to an intra-patient registration scenario, i.e. the same anatomical landmarks can be found in the follow-up images. Following a first anatomic landmark based registration, an extracted surface, which is constrained by the available anatomical landmarks obtained in the first phase of the method, drives the second phase of the registration. This is a surface registration step that propagates the solution towards matching of the important features over a consistent part of the scalp for a better and extensive fit over the head surface for a refinement of the final affine transformation. Apart from its use in tumor follow-up studies, the proposed rigid registration method can be used as a pre-processing before generic deformable registration applications, which require an initial rigid alignment phase.

1.2 Contributions

In this thesis, we have:

- Extracted five different anatomical landmarks from the head region and proposed novel methods to segment and extract them.

- Defined several geometric features of the anatomy and observed that some of them such as CoS-plane can also be used in other applications.

- Developed an optimization method which refines the result of our anatomical landmark-based registration method using the surface of head.

The proposed method in this thesis is published in [32] and [33].

1.3 Outline

The organization of the thesis is as follows. In Chapter 2, a background on medical image registration is given with the necessary information to follow the thesis. In Section 3.1, the specific anatomical landmarks used in our algorithm and their extraction is described. The proposed registration method based on anatomical landmarks is presented in Section 3.2. The results are demonstrated in Chapter 4 with consistency tests and validation studies, followed by conclusion and discussion in Chapter 5.

Chapter 2

Image Registration Background

In this chapter, image registration background information required to follow the thesis is briefly described. Mathematical formulation of image registration followed by a classification of different methodologies used in medical image registration are presented.

2.1 Mathematical Formulation

Mathematical formulation of image registration is derived from the intuition that the main goal of image registration is to find an appropriate spatial transformation so that a template, also known as moving or transformed image is similar (in the sense of a similarity criterion to be defined) to a reference (fixed) image.

As a mathematical definition of the registration problem: given a reference image $I_1(\mathbf{X})$, moving image $I_2(\mathbf{X})$, and a necessary transformation $T(\mathbf{X})$ where $\mathbf{X} \in \mathbb{R}^{\mathbf{d}}$ is a coordinate variable in d-dimensional Euclidean space, define a similarity measure $S(I_1(\mathbf{X}), \mathbf{I_2}(\mathbf{T}(\mathbf{X})))$, which is optimized with respect to the transformation T.

Therefore, two main components of a registration problem involve defining (i) an error or cost function that measures the similarity or dissimilarity between the two images to be aligned; (ii) a coordinate transformation, which is either parametric or non-parametric.

There are several similarity measures and some of the intensity-based and landmark-based approaches are introduced in the forthcoming sections. Depending on the nature of the problem, the necessary coordinate transformation might be parametric (rigid or affine) or deformable (non-parametric). Two widely used parametric transforms are defined next.

Rigid transformation

$T(\mathbf{X}) = \mathbf{QX} + \mathbf{b}$, where $\mathbf{Q} \in \mathbb{R}^{\mathbf{d}\times\mathbf{d}}$ is orthogonal and $det(\mathbf{Q}) = \mathbf{1}$, and $\mathbf{b} \in \mathbb{R}^{\mathbf{d}}$. This transformation only permits translation and rotation of the coordinates so that it preserves rigidity.

Affine transformation

$T(\mathbf{X}) = \mathbf{AX} + \mathbf{b}$, where $\mathbf{A} \in \mathbb{R}^{\mathbf{d}\times\mathbf{d}}$ is an affine matrix satisfying that $det(\mathbf{A}) > \mathbf{0}$, and $\mathbf{b} \in \mathbb{R}^{\mathbf{d}}$. In addition to the rigid constraints, affine mapping allows scaling and shearing. This type of transformation therefore is more general than a rigid transform. Note that regarding the nature of our registration problem applied to an initial alignment of serial MRI volumes, non-parametric transformations are out of the scope of this thesis, and we will work only with rigid and affine transformations.

2.2 Parametric Image Registration Methods

In a parametric registration, mathematical model of mapping function has a finite number of parameters. Image registration is achieved by finding the optimal parameters of this function for which the similarity between reference and registered image is maximized. In this class of registration, the coordinate mapping usually requires a few number of parameters. For the case of 3D rigid registration, the mapping requires 6 different parameters (3 for rotation and 3 for translation) whereas an affine mapping requires 12 different parameters (3 for rotation, 3 for translation, 3 for scale, and 3 for shear). Estimation of these parameters is usually an ill-posed problem and no unique solution is available. Therefore, registration is still a popular topic, attracting attention of medical imaging community. Two main strategies are described in forthcoming sections: (i)Landmark-based; (ii) Intensity-based registration approaches.

2.2.1 Landmark-based registration

A landmark is typically an outstanding point of an image. Retrospective (soft) landmarks can be derived from anatomical features such as center of eye balls, or image intensity based coordinates such as the points with maximal curvature.

Another methodology involves positioning of fiducial (hard) landmarks. However these landmarks are usually not comfortable for the patient and correct spatial positioning is not always possible, and furthermore, it requires expert knowledge.

Let $M(I_1, j)$ and $M(I_2, j)$ denote the j^{th} landmark coordinate of reference and moving images respectively, where $j = 1, ..., m$, and $m \in \mathbb{N}$ denotes the number of landmarks. Given the landmarks, registration problem is to find the necessary transformation $T : \mathbb{R}^d \longrightarrow \mathbb{R}^d$, such that $M(I_1, j) = T(M(I_2, j))$.

After a mathematical definition of the landmark based registration problem, a distance measure D between the landmark features of a reference and a moving image is to be defined. A typical distance or error measure is the sum of squared distances (SSD) between the reference coordinates and the transformed coordinates:

$$S^{LB} = \sum_{j=1}^{m} \parallel M(I_1, j) - \varphi(M(I_2, j)) \parallel_f^2 \tag{2.1}$$

where $\parallel . \parallel_f$ denotes the norm of the landmark coordinate vector space.

Choosing the mapping function φ as linear (affine) is a popular approach to solve this problem. In this case φ can be expressed as a product of a transformation matrix A and the homogeneous coordinates in the original image. Note that in the case of a linear transformation, dimension of matrix A is $d + 1 \times d + 1$, where the last column of A denotes the translation in homogeneous coordinates. In Equation 2.2, a sample mapping is shown for $d = 3$, where $[x\ y\ z\ 1]^T$ and $[x^{'}\ y^{'}\ z^{'}\ 1]^T$ are the homogeneous coordinates of reference and moving images respectively.

$$\begin{bmatrix} x \\ y \\ z \\ 1 \end{bmatrix} = \begin{bmatrix} a_{11} & a_{12} & a_{13} & t_x \\ a_{21} & a_{22} & a_{33} & t_y \\ a_{31} & a_{32} & a_{33} & t_z \\ 0 & 0 & 0 & 1 \end{bmatrix} \begin{bmatrix} x' \\ y' \\ z' \\ 1 \end{bmatrix} \tag{2.2}$$

Hence, Equation 2.1 can be expressed in terms of matrices such that,

$$S^{LB} = \sum_{j=1}^{m} \parallel \mathbf{X_j} - \mathbf{A}\mathbf{X_j}^{'} \parallel_{\mathbf{f}}^{\mathbf{2}} \tag{2.3}$$

where $\mathbf{X_j}$ and $\mathbf{X_j}^{'}$ are the homogeneous coordinates of the landmarks for the reference and the moving image respectively. This is known as a least squares

problem, and optimal parameters can be obtained using several numerical solutions. We will present one example numerical solution in Section 3.2.1. Other examples can be found in [1].

2.2.2 Intensity-based registration

In this section we investigate several similarity measures to find an optimal linear registration as well as the numerical solutions to solve for the necessary transformation.

It is difficult to choose an appropriate similarity measure for the registration problem. Usually performances of several similarity measures are compared to choose the best one for the problem. Differentiability of the similarity measure is also an important issue for optimization to achieve the solution in a fast and efficient manner. In the forthcoming sections intensity difference-based, correlation-based, and mutual information-based similarity metrics are discussed in detail.

SSD-based registration

This approach is based on the minimization of intensity differences of reference image $I_1(\mathbf{X})$ and the moving image $I_2(T(\mathbf{X}))$. Intensity similarity measure a.k.a. sum of squared distances (SSD) over the image domain $\Omega : \mathbb{R}^d \Longrightarrow \mathbb{R}$ is defined in Eq.2.4

$$S^{SSD} = \frac{1}{2} \int_{\mathbb{R}^d} (I_1(\mathbf{X}) - \mathbf{I_2}(\mathbf{T}(\mathbf{X})))^{\mathbf{2}} \mathbf{dX} \tag{2.4}$$

There are variety of methods that can be used to solve these kinds of minimization problems. Direct methods and steepest descent methods might be relatively slow for high resolution images. On the other hand second order derivative-based methods are usually problematic and not stable for many applications due to low signal-to-noise ratio (SNR). Gauss-Newton method is mostly used to solve these kinds of minimization problems.

Normalized cross correlation-based registration

Correlation is an information measure for linear independence and it can be defined by Equation 2.5. For the registration problem the goal is to maximize correlation

between the images R and T:

$$Corr_{R,T}(\mathbf{Y}) := \int_{\mathbb{R}^{\mathbf{d}}} \mathbf{R}(\mathbf{X})\mathbf{T}(\mathbf{X}-\mathbf{Y})\mathbf{dx} \tag{2.5}$$

Correlation can also be considered as an L_2-inner product $\langle ., . \rangle$ between R and T. In practice images R and T are normalized so that they are of unit norm and normalized correlation is the cosine of the angle between R (reference) and T (moving) images. Using the statistics (mean μ, standard deviation σ) of the two images, correlation coefficient is defined by:

$$\gamma(R, T; \mathbf{Y}) := \langle \frac{\mathbf{R} - \mu(\mathbf{R})}{\sigma(\mathbf{R})}, \frac{\mathbf{T_Y} - \mu(\mathbf{T_Y})}{\sigma(\mathbf{T_Y})} \rangle_{\mathbf{L_2}} \tag{2.6}$$

where $T_{\mathbf{Y}}(\mathbf{X}) = \mathbf{T}(\mathbf{X} - \mathbf{Y})$. Hence, correlation-based similarity measure is exactly the correlation coefficient between the reference $I_1(\mathbf{X})$ and registered $I_2(T(\mathbf{X}))$ images as in Equation 2.7.

$$S^{NCC} := \langle \frac{I_1(\mathbf{X}) - \mu(\mathbf{I_1})}{\sigma(I_1)}, \frac{I_2(T(\mathbf{X})) - \mu(\mathbf{I_2}(\mathbf{T}(\mathbf{X})))}{\sigma(I_2(T(\mathbf{X})))} \rangle_{L_2} \tag{2.7}$$

Mutual information-based registration

Mutual information (MI) is a measure of the entropy and it was originally defined in the field of information theory. For the registration problem, the goal is to maximize mutual information so that the dispersion of joint density between the reference image and moving image is minimal. It can also be inferred that when the mutual information is maximal, two images are maximally related, i.e. their degree of dependence is maximized.

Mathematical definition of the (differential) entropy is given in Equation 2.8, where, $q \in \mathbb{N}$ and $\rho : \mathbb{R}^q \implies \mathbb{R}$ is a density of image intensities i, on $\mathbb{R}^q$, with $\rho(i) \geq 0$, and $\int_{\mathbb{R}^q} \rho(i)di = 1$.

$$H(\rho) := -\int_{\mathbb{R}^q} \rho(i) \log \rho(i) di \tag{2.8}$$

Mutual information measure between two different images R and T, depends on the entropy of joint density $\rho_{R,T}$ and entropies of the marginal densities ρ_R and ρ_T , and is defined as:

$$S^{MI} := H(\rho_R) + H(\rho_T) - H(\rho_{R,T}) \tag{2.9}$$

where ρ_R, ρ_T, and $\rho_{R,T}$ denote the intensity distributions of R, T, and the joint intensity distributions (joint histogram), respectively. Mutual information is usually normalized, and normalization can be achieved by several approaches. One popular approach is to divide the MI by the sum of marginal entropies such that,

$$S^{NMI} := \frac{H(\rho_R) + H(\rho_T) - H(\rho_{R,T})}{H(\rho_R) + H(\rho_T)} := 1 - \frac{H(\rho_{R,T})}{H(\rho_R) + H(\rho_T)} \ . \tag{2.10}$$

Chapter 3

Anatomical Landmark Based Registration

In this chapter, we present our novel landmark extraction steps in detail with the necessary preliminary features in Section 3.1. Proposed anatomical landmark-based registration method is described in Section 3.2.1. At the end of this chapter surface based refinement method is presented in Section 3.2.2. In Figure 3.1 flow chart diagram of the algorithm is depicted.

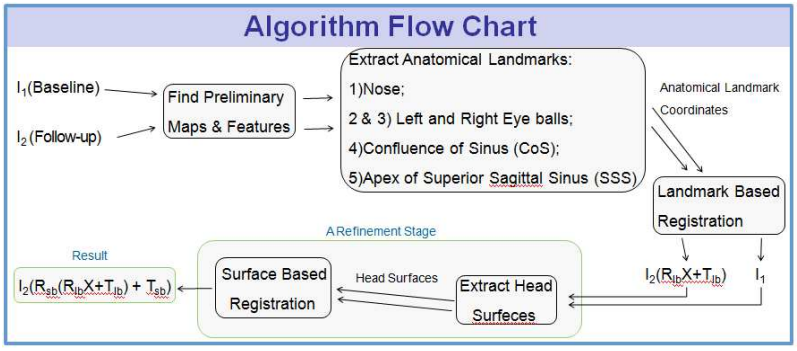

Figure 3.1: Algorithm Flow Chart

Standard coordinate planes and their orientations relative to the human body used in medical imaging is shown in Figure 3.2.

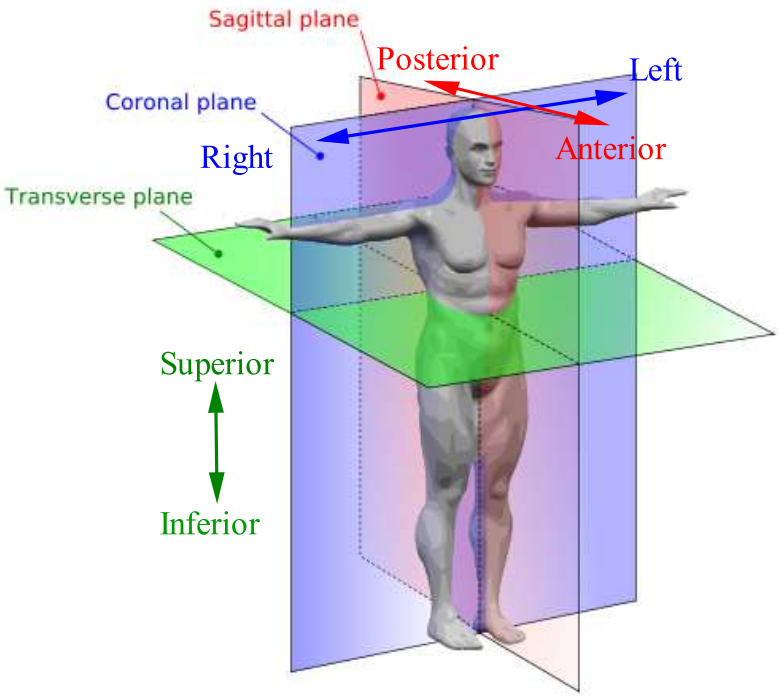

Figure 3.2: Plane orientations used in medical imaging [adaptod from Wiki:HumanAnatomy]

3.1 Extraction of Anatomical Landmarks

The first step of the proposed registration algorithm involves extraction of anatomical brain landmarks on given CE-T1 MRI volumes. Thus, a patient-specific coordinate system, which can be invariably found on all human brain images, is obtained based on a set of selected anatomical landmarks. In this thesis, we proposed to extract and utilize nasal bone tip, center of two eyeballs, confluence of sinus, and apex of superior sagittal sinus. The landmark selection process, i.e. determining brain landmarks that can be reliably observed and computationally extracted, was carried out jointly with the radiologists in the team. In Section 3.1.1, preliminary features required to extract selected anatomical landmarks are presented followed by extraction of each of the five landmarks on Section 3.1.2 to 3.1.5.

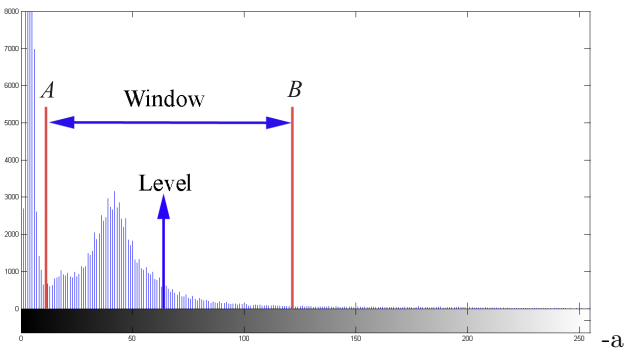

-a

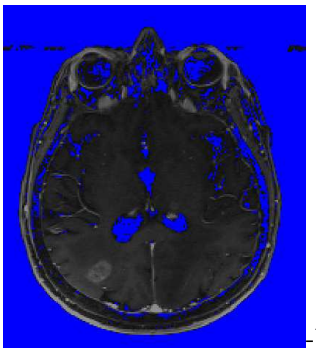
-b

Figure 3.3: a)Histogram based window-level filter (A denotes background noise level, B denotes maximum intensity level) b)Filter output with background noise (blue).

3.1.1 Preliminary maps and features

Binary head mask

A simple binary head mask consisting of the full head including the outer skin of the human body is constructed first. Initially, a histogram based window-level filter is used such that minimum intensity level of the window (background noise level in the image) is calculated from the local minimum that comes after first local maxima of the histogram whereas the maximum intensity level of the window is located at the intensity for which histogram count is less than 1% of local maxima that comes after detected noise level. A typical intensity histogram froma a CE-T1MRI sice is shown in Figure 3.3 which depicts both the background noise level and maximum intensity level labeled with A and B, respectively.

Figure 3.4 shows images from consecutive steps of the proposed binary head mask computation. Histogram filtered image is then used in a canny edge detection [7]. Then the canny edge map is dilated (Figure 3.4-c) so that region growing algorithm which will be seeded from image grid boundaries does not leak into the head region. Region growing algorithm connects the background pixels and those unreachable pixels are marked as foreground of the binary map, and then eroded with the same size of dilation forming final head mask (Fig.3.4-d).

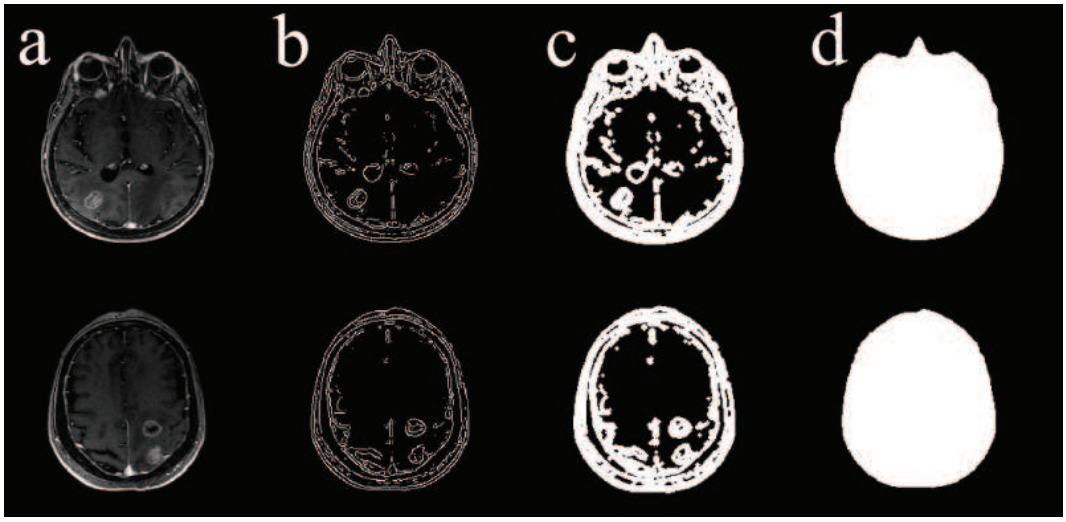

Figure 3.4: Binary head formation steps for two different axial slices: a)Original MRI Slice, b)Canny edges, c)Dilated canny edges, d)Obtained head mask.

Anterior tip points

Anterior tip point of each axial slice is the nearest point of binary head mask to the top most row of the slice. It is detected with a linear search in rows starting from the top most row. If there are more than one marked pixel on a given row, then mid point of these pixels is marked as an anterior tip point. Fig.3.5 demonstrates sample slices with tip points marked as (+) sign.

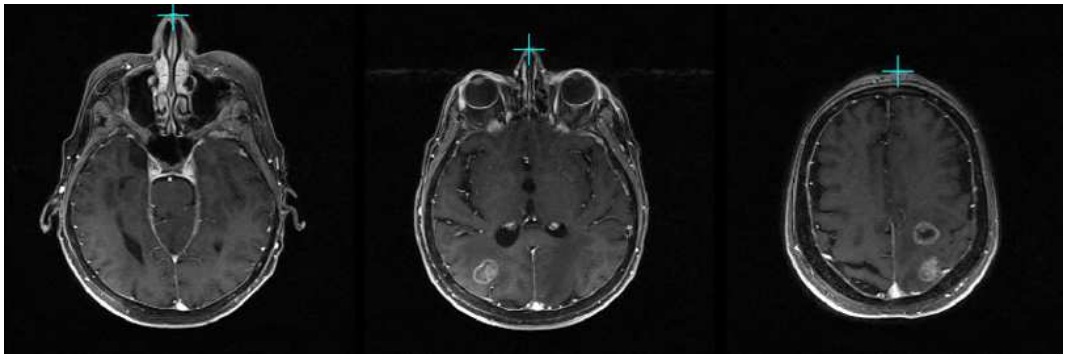

Figure 3.5: Anterior tip points of sample slices.

Axial Tilt Problem

MRI scanner can handle acquisition in arbitrary plane orientations. The acquisition can be performed in any orientation such as in an axial direction, parallel to AC-

PC (anterior commissure - posterior commissure) line which refers to Talairach coordinate system [15]. However AC-PC alignment is not always carried out, and the acquisition orientation can be different for different acquisitions. In our clinical partner site (Anadolu Medical Center), CE-T1 MRI is directly acquired with no acquisition orientation adjustment. The consequence of this is an occasional axial tilt problem which depends on the patients position in MRI head coil. Figure 3.6 illustrates the problem and shows different positioning of the patient. This problem may introduce errors for our anatomical landmark extraction algorithms. A solution to this problem is presented in Section 3.1.2.

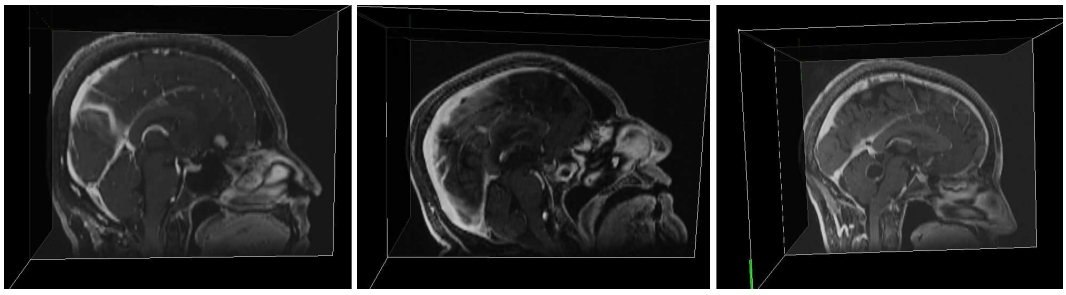

Figure 3.6: Axial tilt problem in MRI volume acquisition: Normal (left), tilt up (middle), tilt down (right).

Symmetry Line Calculation

Mid-sagittal symmetry line is defined such that it passes through the anterior tip point and center of mass using 1^{st} order image moments of axial binary head mask slice. This is indeed a rough estimate of the natural symmetry of human head (brain). Fig.3.7 depicts sample symmetry line estimates, which will then be used in anatomical landmark extraction steps.

Specific distances and definitions

Mid-sagittal symmetry line facilitates several geometric features (see Figure 3.8): p_1, the point with the maximum perpendicular distance to the symmetry line, p_2, the most anterior point of eye balls, and d_1 and d_2 are perpendicular distances from p_1 and p_2, to the symmetry line (Fig.3.8).

The ratio given in Equation 3.1 is observed to be a biometric constant with a certain mean and variance (0.42 ± 0.01) which was measured over 20 MRI scans.

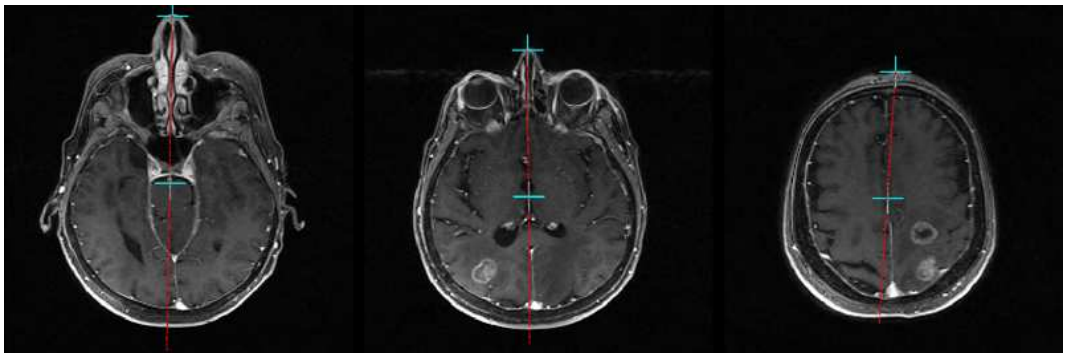

Figure 3.7: Sample symmetry line estimates, depicted as a red line.

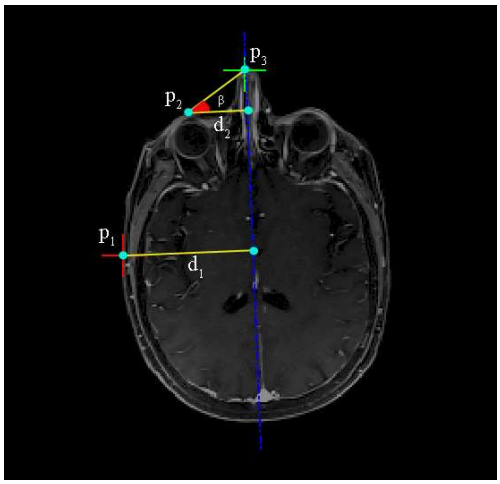

Figure 3.8: Geometric features (p_1, p_2, d_1, and d_2, and the angle β)

$$c := \frac{d_2}{d_1} \tag{3.1}$$

In addition we defined an angle β between the line passing through p_2 and anterior tip point (p_3), and the line passing through p_2 and perpendicular to the symmetry line.

3.1.2 Nasal Bone from Nose

Nose landmark is located using the angle β feature, which is defined in the previous section and depicted in Figure 3.8. The value of $\tan\beta$ is examined for axial slices. Figure 3.9 depicts a 3D representation of nose tip points and red-to-blue (0.0 to 1.0) color code represents value of $\tan\beta$ for the corresponding axial slice. Starting from the top most axial slice, first nose tip point is detected where $\tan\beta$ is greater than a certain threshold, and lower end of nose tip points is marked where the

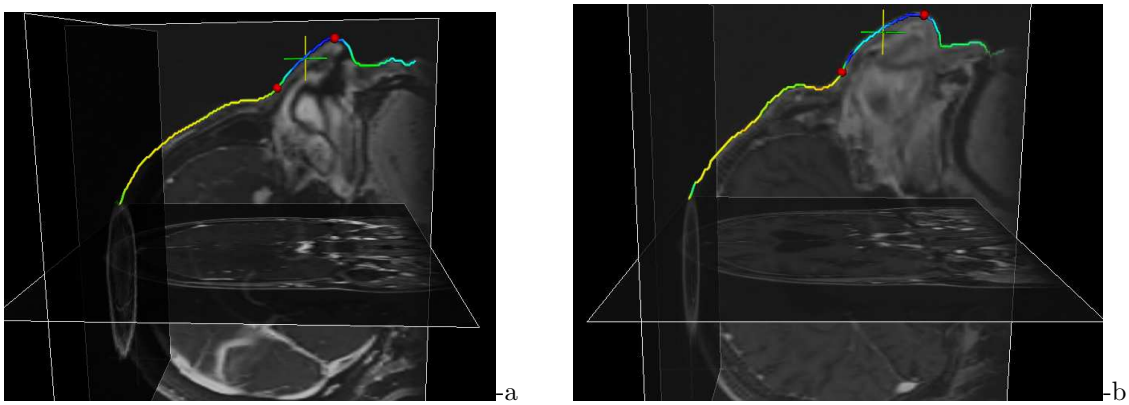

Figure 3.9: Nose feature a)Case 1, b)Case 2.

outermost anterior tip point is reached. In Figure 3.9 small red spheres represents the beginning (superior) and final (inferior) points of detected nose tips. Finally, a single nose landmark is marked at the center of detected nose tip points, which is close to the tip of nasal bone (marked with a (+) sign in Fig.3.9).

A Solution to Axial Tilt Problem

Axial tilt problem defined in Section 3.1.1 can be resolved using the nose feature. It is observed that the nose line connecting the upper and lower nose tip points identifies the degree (angle) of tilt, that is, if the nose line is closer to the axial plane than the coronal plane, or vice-versa, then there exists an axial tilt problem (Fig.3.10). The solution to this problem can be achieved by rotation of the MRI volume about the grid center, so that the projections of the nose line onto the coronal plane and axial plane are equal in length.

3.1.3 Eye Balls

An eye ball is segmented using a sphere model, which is initiated at a seed point based on the nose feature. Two seed coordinates for the left and right eye balls are first estimated on the top most axial slice of the nose, then given d_1, d_2 is estimated using the ratio c (Eq. 3.1). Using the anatomical knowledge that physical radius of an eyeball is roughly 10 mm, the seed is initialized 10 mm away from p_2 towards the symmetry line to ensure that the seed point falls in the eye ball region. Sample seeds are shown as yellow (+) signs in the middle column of Figure 3.11. Initialized

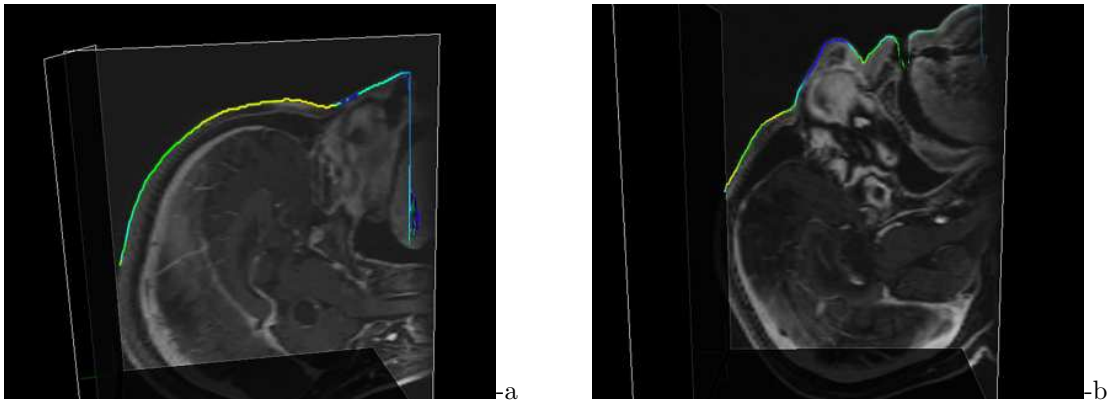

Figure 3.10: Nose feature to resolve axial tilt problem. a)Tilt is downward, b)Tilt is upward.

sphere parameters (center and radius) are evolved until convergence with ordinary differential equations derived to maximize the difference between the mean intensity statistics inside and outside the sphere within a band around its surface as explained next.

Region-Based Sphere Evolutions

Given an image volume $I : \Omega \longrightarrow \mathbb{R}^3$, the goal is to find a volumetric sphere surface $\mathbf{C} \in \Omega$, and the mapping $\mathbf{C} = \boldsymbol{X}$ propagates on the image domain Ω with a region-based energy:

$$E(\lambda) = \int_{\mathbf{\Omega}} f(\boldsymbol{X}, \lambda) dx. \tag{3.2}$$

where $f = f_{in} - f_{out}$, and f_{in} and f_{out} are the region descriptors inside and outside of the sphere, and λ is the set of $\lambda^j \in \{r, a, b, c\}$, $j = 1, ..., 4$, which are the sphere parameters given in Equation 3.3, respectively, and $\boldsymbol{X} \in \Omega$ is the coordinate variable of the sphere. The parametric sphere $\mathbf{C}$ is updated by $\frac{\partial \mathbf{C}}{\partial t} = f(\boldsymbol{X})\mathbf{N}$, where $\mathbf{N}$ denotes the unit normal to $\mathbf{C}$.

The parametrization of sphere coordinates $\boldsymbol{C}(s, p) = \boldsymbol{X}$ with $s \in [0, 2\pi)$ and $p \in [0, \pi)$, given its radius r and translation vector $t = (a, b, c)^T$, is given by:

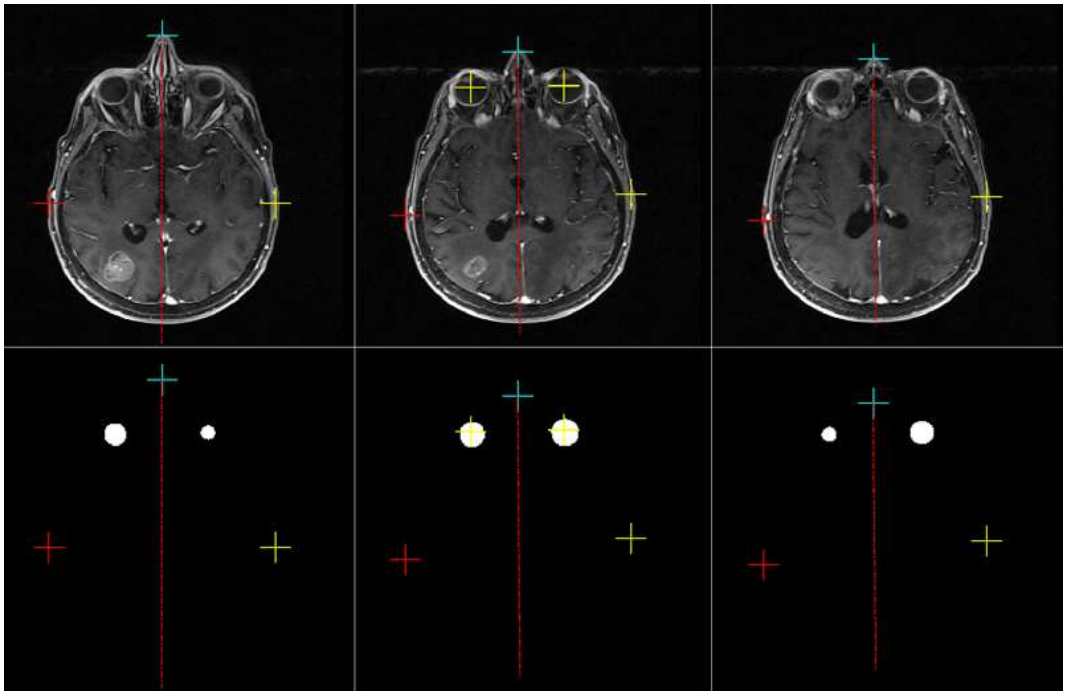

Figure 3.11: Sample axial slices from eye region and corresponding segmentation result is below. Eye seeds are shown on the central figure with yellow (+) sign.

$$\boldsymbol{X}\,(s,p) = r \begin{pmatrix} cos(s)\ sin(p) \\ sin(s)\ sin(p) \\ cos(p) \end{pmatrix} + \begin{pmatrix} a \\ b \\ c \end{pmatrix} \tag{3.3}$$

Using this parametrization, the variation of the energy in Eq.3.2 w.r.t. sphere parameters $\lambda^j \in \{r, a, b, c\}$, $j = 1, ..., 4$ yields the gradient flows:

$$\frac{d\lambda^j}{dt} = -\oint_{\boldsymbol{C}} f(\boldsymbol{X}\,) < \frac{\partial \boldsymbol{X}}{\partial \lambda^j}, \mathbf{N} > dpds\ , \tag{3.4}$$

which provides us with equations of the evolution of the 3D sphere parameters λ^j, hence the update step for the eye ball sphere. We solve the ordinary differential equations of each parameter update equation until steady state. The obtained values of the parameters $\lambda^j \in \{r, a, b, c\}$ define the final two spheres, one for left and one for right eyeball, which leads to a good fit to the two eyeball anatomy. Sample eyeball sphere results are shown in Figure 3.12.

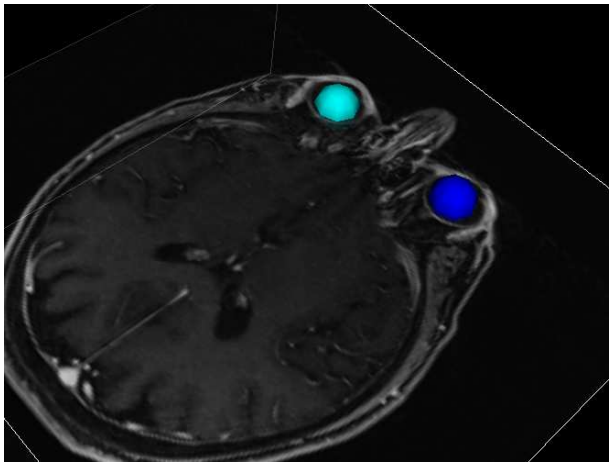

Figure 3.12: A sample results of sphere evolution for eye balls.

3.1.4 Confluence of Sinus

Confluence of sinus is conjunction point of the superior sagittal sinus and transverse sinus. A distinguishing feature of the confluence of sinus is that it is located where the superior sagittal sinus bifurcates as depicted in Fig.3.13.

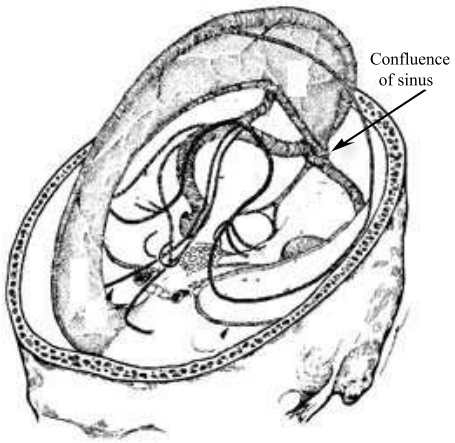

Figure 3.13: Cerebral venous system (figure adapted from Osborn A. Diagnostic neuroradiology. St. Louis: Mosby, 1994).

Confluence of sinus (CoS) detection starts by locating a seed point on the superior sagittal sinus. As depicted in Fig.3.14, the seed point is searched on the axial slice at eye ball centroid level and towards the posterior part of binary head mask's center of mass within a finite width of the mid-sagittal symmetry line with respect to a maximum brightness criterion.

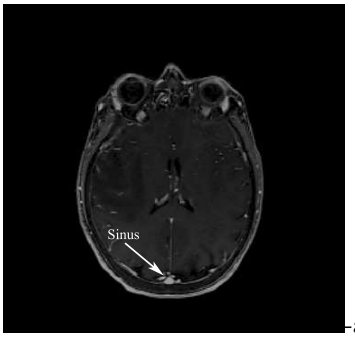

a

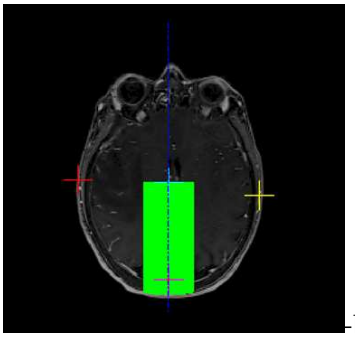
b

Figure 3.14: Seed point search region over a T1-MRI slice for sinus map extraction.

After the seed is initialized over the sagittal sinus (Fig.3.14-b marked with a (+) sign), mean μ and standard deviation σ values over a small window are calculated, and a 3D region growing is performed with an initial downward motion and a growing criterion of accepting pixel intensities greater than $\mu - \sigma$. The result of segmentation by region growing produces a sinus map, as visualized in Fig.3.15 with a height map overlay.

Next, the segmented sinus map is analyzed using region moments of axial slices. In this study, we defined the confluence of sinus at the slice, which has the maximum variance in the left-right direction. This is performed using a covariance matrix formed by second order central moments of the sinus map over each slice: $[\mu_{20}, \mu_{11}; \mu_{11}, \mu_{02}]$. This matrix is then decomposed into its eigenvectors and eigenvalues $[\lambda_1\ \lambda_2]$ where $\lambda_1 \geq \lambda_2$, using singular value decomposition. The ratio between the two eigenvalues $(\frac{\lambda_1}{\lambda_2})$ is examined and when it exceeds a certain threshold the slice of CoS is located (Z coordinate), and axial (X and Y) coordinates of CoS is calculated using the average center of mass of the sinus map. Fig.3.15 depicts detected CoS landmarks from two different cases where red-to-blue surface color map represents the CoS feature $(\frac{\lambda_1}{\lambda_2})$. It can be observed that the bifurcation slice is indicated by the abrupt $\frac{\lambda_1}{\lambda_2}$ change also coded by the color map change into blue.

3.1.5 Apex of Superior Sagittal Sinus

For an even sampling of landmarks over the brain, a final anatomical landmark is selected at the apex of the superior sagittal sinus. Similar to extraction of CoS, superior sagittal sinus (SSS) surface is delineated by region growing constrained

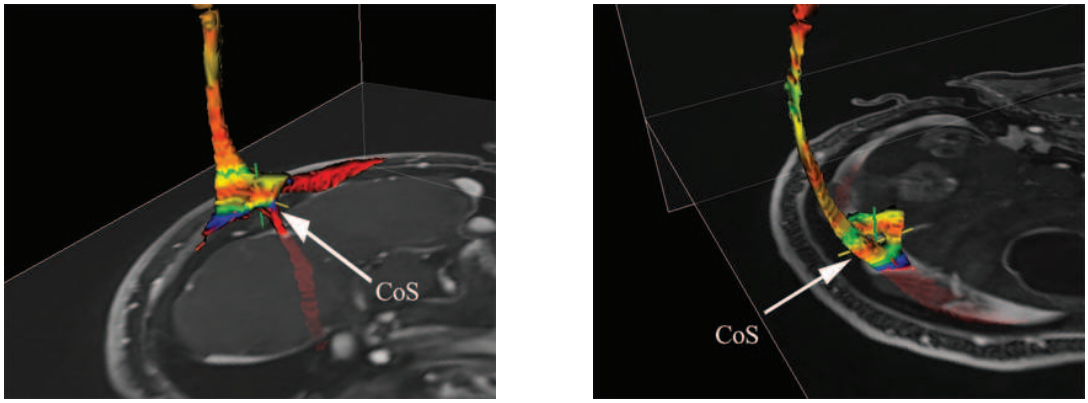

Figure 3.15: Sinus map and CoS are shown from two different cases. Red-to-blue color indicates the CoS feature.

this time by an initial motion towards superior (upward) direction. A sample SSS extracted from a CE-T1 MRI volume is shown in Fig.3.17. We define a plane constructed from the three anatomical landmark points: CoS, and the two eye ball centroids, as visualized in Fig.3.16. This plane, which we called CoS-Eyeballs plane, is observed to be parallel to the AC-PC line used in Talairach coordinate system by the radiologist in our project team. SSS feature is selected as the point on the SSS having a maximum distance to this plane. This feature is visualized on Figure 3.17 with a red-to-blue color map on the SSS surface. For robustness, the center of a cloud of points with distances greater than 99% of the maximum distance is marked as the apex of superior sagittal sinus, depicted with a cross bar in Figure 3.17.

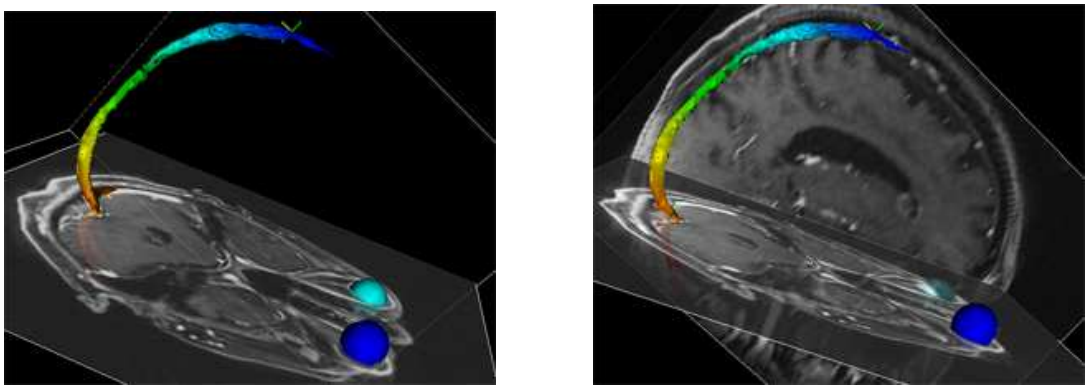

Figure 3.16: CoS-Eyeballs planes from two different viewpoints.

Finally, all five anatomical landmarks are extracted and visualized in Figure 3.18 from two different viewpoints for a sample patient CE-T1 MRI scan.

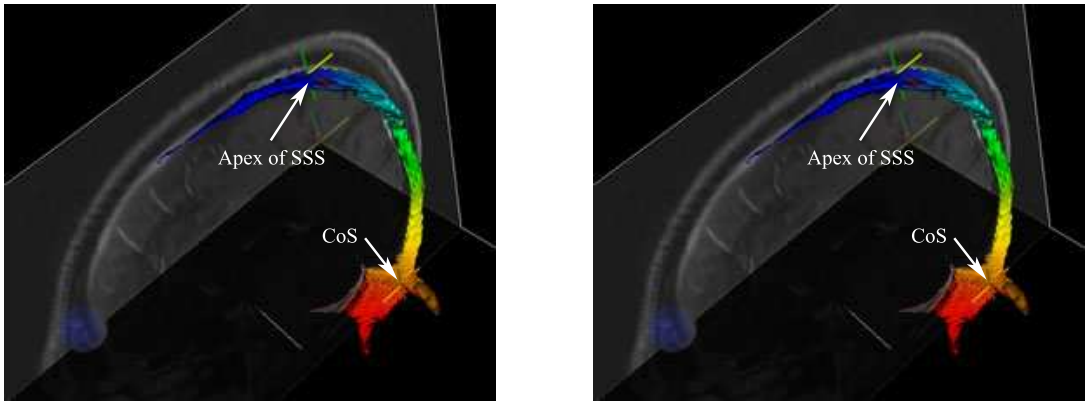

Figure 3.17: Apex of Superior Sagittal Sinus is marked with axis bar widget. Red-to-blue color represents SSS map.

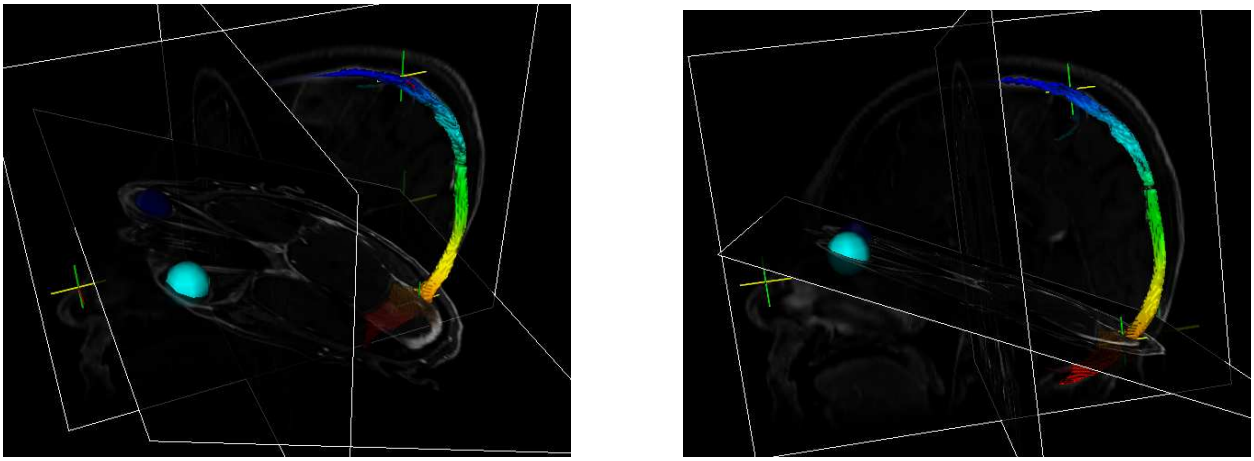

Figure 3.18: All five extracted anatomical landmarks visualized together.

3.1.6 Dens Axis and Brain Stem

Dens axis and brain stem are two different anatomical structures, which we attempted at extracting in order to define new landmarks. However, these structures are located at inferior of the brain where signal to noise ratio (SNR) is usually low. Moreover, there exists strong inhomogeneity artifacts on these slices. In this section some approaches to extract these structures are demonstrated and discussed. However, solutions are not in 3D and experimental results were not satisfactory. Therefore, we did not utilized these two anatomical structures as landmarks in our registration. For completeness, we report our methods in extraction of these structures below.

Dens Axis

Dens axis is a part of the second cervical vertebra (C2) and it has a tooth-like shape joining the C2 and first cervical vertebra (C1). It has a certain shape that it is circular on axial slices (Figure 3.19). For this reason we worked on axial slices where dens axis exists.

In this part we define a rectangular region of interest (ROI) with the center of mass of the axial slice is the center of ROI (Figure 3.20). We defined a circular shape for dens axis model and searched over the ROI with this model having the minimum mean intensity. In Figure 3.20 a sample result is depicted.

This method has several problems. First of all there may be other similar structures with low intensities and secondly dens axis may be elliptical instead of perfect circular shape. Inhomogeneity artefacts also affect the algorithm. Moreover our solution requires an ROI initialization and correct axial slice must be selected manually.

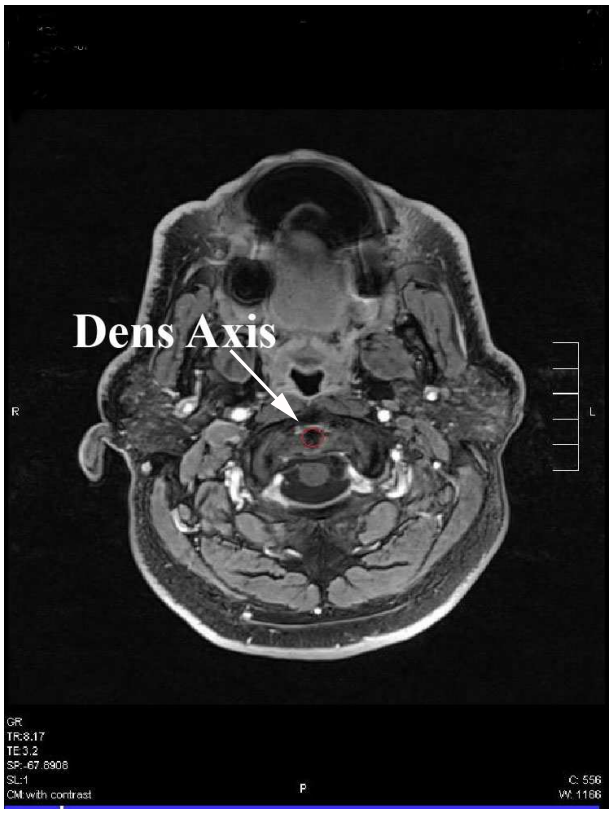

Figure 3.19: Sample result for dens axis

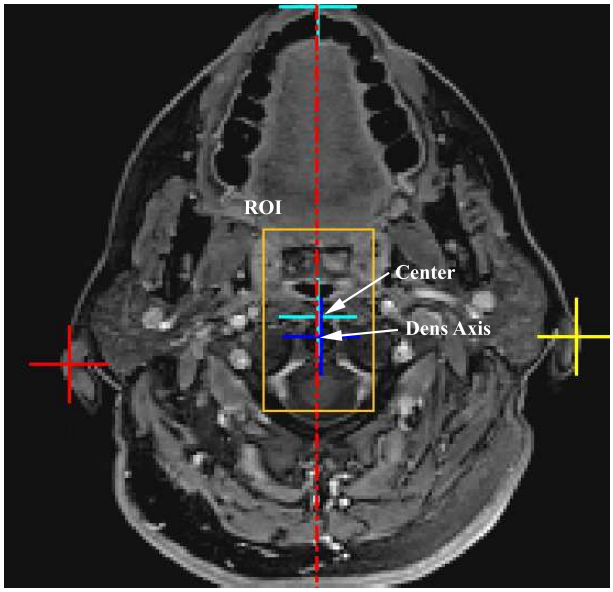

Figure 3.20: Dens Axis

Brain Stem

Brain stem is the structure which is a part of the spinal cord and it connects the spinal cord to the brain. This structure can be seen on the same axial slice of dens axis. It has a circular shape on axial slice and it is surrounded by a spinal fluid which has lower intensity values corresponding to the brain stem.

Using the same ROI that we defined for dens axis, we searched for the brain stem using Hough transform [25] and we calculated mean intensity of circular shapes with different radius (Figure 3.21). We see that for the brain stem, mean intensity decreases and standard deviation (std) increases with increasing radius. Hence, we calculated mean/std value for brain stem. We depicted a sample result in Figure 3.22.

3.2 Registration Method

3.2.1 Anatomic Landmark-based Registration

In the specific problem of registering serial MR images, a fixed reference volume is usually the baseline MRI volume, which is the first MRI acquisition of the patient. The baseline MRI volume is to be rigidly aligned with a moving volume, which is

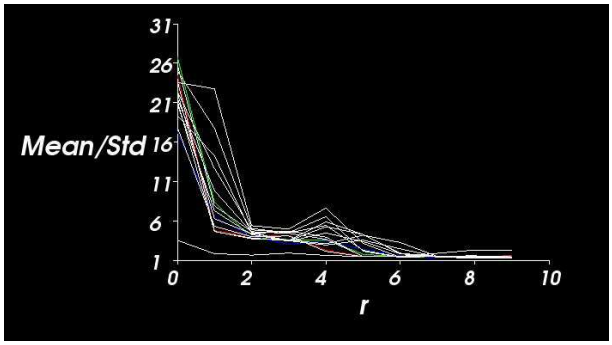

Figure 3.21: Circular hough transform for brain stem

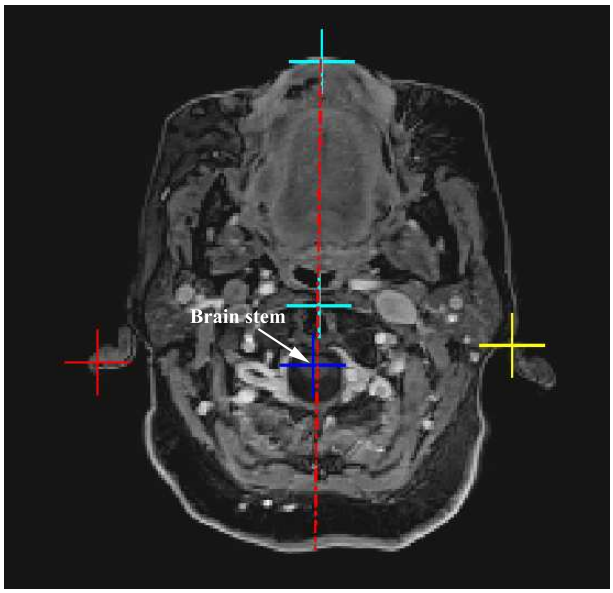

Figure 3.22: Sample result for brain stem

usually a follow-up MRI volume, i.e. a second MRI acquisition of the patient after sometime has passed after the baseline scan. Typical follow-up times are on the order of months for the brain tumor follow-up routine.

For a landmark based approach, a 3D affine transformation ($\boldsymbol{T} = \boldsymbol{A}_{3\times3}, \boldsymbol{t}_{3\times1}$) is estimated by minimizing the sum of squared distances between the extracted anatomic landmark coordinates of the fixed volume and the moving volume. $\boldsymbol{A} \in GL(3)$, the general linear group, i.e. $\boldsymbol{A}$ is an invertible 3×3 matrix. Coordinates are all in world coordinates and the centroid of the landmarks is chosen as the reference point for each MR volume. Translation component $\boldsymbol{t}$ of $\boldsymbol{T}$ is directly obtained from the difference of the centroids of the five landmarks that belong to the fixed and the

moving volumes.

Let $\boldsymbol{X}_f = [x_f, y_f, z_f]^T$ be a fixed landmark coordinate, $\boldsymbol{X}_m = [x_m, y_m, z_m]^T$ be its corresponding moving landmark coordinate, and $\boldsymbol{A}$ is the affine transformation between the two. Then, $\boldsymbol{A}$ can be obtained as the solution of the least squares estimation problem: $\boldsymbol{A} = \arg\min \sum_{i=1}^{n=5} ||\boldsymbol{X}_f^{\,i} - \boldsymbol{A}\,\boldsymbol{X}_m^{\,i}||^2$. After taking the derivative with respect to the unknown $\boldsymbol{A}$, equating to zero, and re-arranging the terms yields:

$$\boldsymbol{N} = \begin{bmatrix} \boldsymbol{M} & \boldsymbol{0} & \boldsymbol{0} \\ \boldsymbol{0} & \boldsymbol{M} & \boldsymbol{0} \\ \boldsymbol{0} & \boldsymbol{0} & \boldsymbol{M} \end{bmatrix}, \quad \boldsymbol{N}\,\boldsymbol{a} = \boldsymbol{b} \quad , \tag{3.5}$$

, where $\boldsymbol{0}$ is a 3×3 all zeros matrix, and

$$\boldsymbol{M} = \begin{bmatrix} \sum_i^n x_m^2 & \sum_i^n x_m y_m & \sum_i^n x_m z_m \\ \sum_i^n y_m x_m & \sum_i^n y_m^2 & \sum_i^n y_m z_m \\ \sum_i^n z_m x_m & \sum_i^n z_m y_m & \sum_i^n z_m^2 \end{bmatrix} \quad , \tag{3.6}$$

and

$$\boldsymbol{b} = \begin{bmatrix} \sum_i^n x_f x_m, \Sigma x_f y_m, \sum_i^n x_f z_m, \sum_i^n y_f x_m, \Sigma y_f y_m, \sum_i^n y_f z_m, \sum_i^n z_f x_m, \Sigma z_f y_m, \sum_i^n z_f z_m \end{bmatrix}^T \quad . \tag{3.7}$$

The parameter vector $\boldsymbol{a} = [a_{11}, a_{12}, a_{13}, a_{21}, a_{22}, a_{23}, a_{31}, a_{32}, a_{33}]^T$ of the matrix $\boldsymbol{A}$ can be calculated as $\boldsymbol{a} = \boldsymbol{N}^{-1}\boldsymbol{b}$.

Final affine solution is projected to an orthogonal matrix space using a polar decomposition: $\boldsymbol{A} = \boldsymbol{Q}\,\boldsymbol{S}$, where $\boldsymbol{Q}$ is the closest possible orthogonal matrix to $\boldsymbol{A}$ in the sense of Frobenius norm, and $\boldsymbol{S}$ is a positive-definite symmetric matrix. The factor $\boldsymbol{Q}$ can be calculated using a singular value decomposition of $\boldsymbol{A} = \boldsymbol{U}\,\boldsymbol{K}\,\boldsymbol{V}^T$, where $\boldsymbol{Q}$ is then selected as $\boldsymbol{Q} = \boldsymbol{U}\,\boldsymbol{V}^T$ [26]. The resulting $\boldsymbol{Q}$ is always a rotation matrix with a positive determinant since known anatomical correspondences ensure that no reflection can occur.

At the end of the anatomical landmark based registration described above, the rotation matrix $\boldsymbol{Q}$ is obtained, and used as an initial value in the next phase of the registration as explained next.

3.2.2 Refining Head Surface Registration

The result of landmark based registration is further refined for an improved and extensive fit of the head/scalp surface of the moving image to that of the fixed

image. The binary head masks of fixed and moving volumes confined by the CoS-Eyeballs plane, defined in Section 3.1.5, are represented as the zero-level sets of two signed distance functions Φ^f and Φ^m, respectively. Figure 3.23 shows two sample constrained head surfaces visualized by VTK marching cubes algorithm [29] as the iso-surface of the signed distance function representation.

The sum of squared differences between the two signed distance functions can be defined as:

$$E(g) = \int_{\Omega} [\Phi^f(\boldsymbol{X}) - \Phi^m(g(\boldsymbol{X}))]^2 d\boldsymbol{X} \tag{3.8}$$

where Ω is the domain of the image volume, which is limited to the constrained head region. The error functional E is minimized to estimate a rigid transform $g(\boldsymbol{X}) = \boldsymbol{R}\boldsymbol{X} + \boldsymbol{t}$. The 3D rotation $\boldsymbol{R}$, and 3D translation $\boldsymbol{t}$ constitute the rigid transformation parameters $g_i,\ i = 1, ..., 6$, which are obtained by solving the ordinary differential equations (ODEs):

$$\frac{\partial g_i}{\partial t} = \int_{\Omega} [\Phi^f(\boldsymbol{X}) - \Phi^m(g(\boldsymbol{X}))] < \nabla \Phi^m(g\boldsymbol{X}), \frac{\partial g(\boldsymbol{X})}{\partial g_i} > d\boldsymbol{X} \tag{3.9}$$

where $< \cdot, \cdot >$ denotes the Euclidean inner product in R^3, and ∇ denotes a gradient operator. The ODEs in Equation 3.9 were obtained by deriving the gradient descent equations of E in Equation 3.8, with respect to g_i. We utilized the exponential coordinate representation for the 3D rotation (e.g. see [30]). For details of rotation derivatives with respect to exponential coordinates we refer to [31]. The initial conditions were set to the translation vector and the rotation matrix obtained from Section 3.2.1. At the steady-state of the ODE solutions, the final translation and rotation parameters are obtained as the output rigid transform of the proposed method.

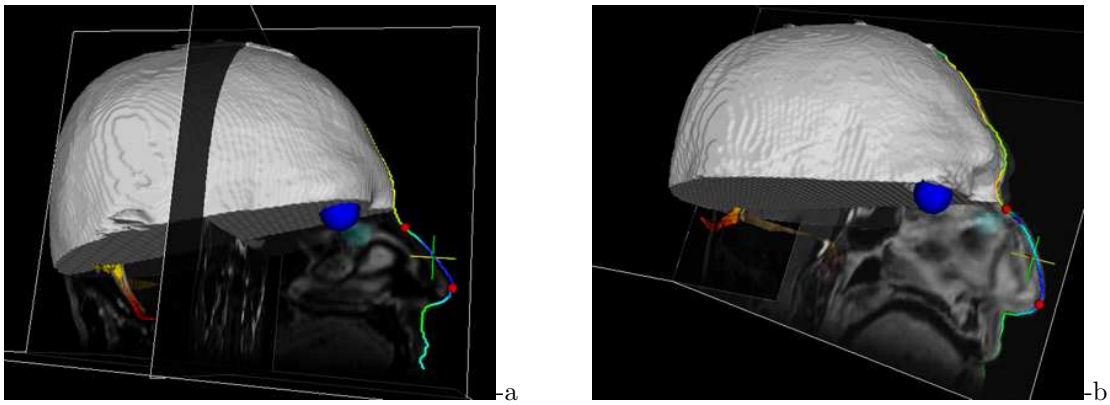

Figure 3.23: Head surface confined by CoS-Eyeballs plane: a)Case 1 b)Case 2.

Chapter 4

Experimental Results

The experiments were carried out over 7 follow-up MRI scans obtained from our clinical partner hospital (Anadolu Medical Center). The study was approved by the IRB (Internal Review Board) of the hospital for ongoing research projects [1] . The proposed method is validated in various ways:

- Over synthetically transformed MRI scans,
- Real MRI baseline and follow-up scans,
- A manually expert marked data set,
- A data set with non-invasive fiducial landmarks attached to a patient's head.

CE-T1 MRI volumes with 1mm slice thickness and axial resolution of 0.5mm are acquired from a Siemens 1.5 Tesla MR system. The proposed registration method is fully implemented in C++ environment, using Qt [27] and VTK [29] libraries for visualization. The parameters of the algorithm are fixed over all experiments as follows:

- The threshold of $\tan\beta$ is 0.40 in Section 3.1.2,
- The width of CoS seed search bounding box is 25mm,
- Window size for region growing parameter calculation is 7×7,
- Exceeding level of $\frac{\lambda_1}{\lambda_2}$ is 10 in Section 3.1.4.

[1]This work was partially supported by Tubitak Grant No:108E126, and EU FP7 Marie Curie Grant No: PIRG03-GA-2008-231052.

4.1 Consistency Tests

Consistency testing method proposed by Jenkinsen et al. [24] provides a quantitative synthetic validation procedure for our method. In this test, new images are created using several pre-determined transformations with rotation and translation. All transformed images are then registered to the reference image. If the method is consistent, prescribed and calculated transformations should be the same. Performance of the proposed method is tested with a consistency dataset containing 8 CE-T1 MRI and their artificially transformed MR volumes with a known transformation matrix constructed by 5 degrees of rotation about Z axis, 5 degrees of rotation about Y axis, and translated by [2,4,-2] mm in this case.

Registration is carried out using anatomical landmarks described in Section 3.2.1, and followed by a surface based refinement procedure described in Section 3.2.2. In an ideal case, prescribed and calculated transformation matrices should be identical. In this experiment we used Jenkinson's RMS error deviation:

$E_{RMS} = \sqrt{\frac{1}{5}r^2 Trace(A^T A) + (t + Ax_c)^T (t + Ax_c)}$

where $A = R_{prescribed} - R_{calculated}$, $t = T_{prescribed} - T_{calculated}$, x_c is world center, and r is estimated brain radius. We used CoS and SSS landmarks to estimate the brain radius such that $r = \|\mathbf{X_{CoS}} - \mathbf{X_{SSS}})\|/\mathbf{2}$.

The proposed method is compared to widely adopted standard rigid registration methods based on minimization of squared intensity differences and cross correlation criterion already implemented in ITK Toolkit (MeanSquaresImageToImageMetric and NormalizedCorrelationImageToImageMetric). Consistency dataset also experimented with expert guided manual landmark based registration. For this experiment experienced radiologist marked five different anatomical locations and necessary rigid body transformation is estimated using the same method described in Section 3.2.1. Observed errors are interpreted as mean ± standard deviation as shown in Table 4.1. It is observed that surface based refinement stage successfully improves the performance of proposed anatomical landmark based registration. Proposed method outperforms intensity based registration techniques. Our results also indicate that manual landmark based registration might be problematic in 3D volume registration particularly when it is hard to locate a landmark in 3D such as brain.

Table 4.1: Transformation error measures on consistency dataset

Registration Method	Error [mm]	Std. dev.
Expert Guided Manual Landmark Based	5.49	2.48
Itk Normalized Cross Correlation	3.82	0.90
Itk Mean Squares	3.31	0.58
Anatomical Landmark Based	3.04	0.94
Anatomical Landmark Based with Surface Refinement	**2.41**	**0.53**

Furthermore, the proposed method (including surface based refinement stage) takes typically 90 seconds of processing time on a personal computer with 3.16 GHz processor, whereas the ITK mean squares error minimization method takes typically 120 seconds, and ITK normalized cross correlation method takes typically 180 seconds of processing time for our datasets and manual landmarking usually takes 6 to 10 minutes. Therefore, proposed method is more efficient in terms of computation times.

4.2 Landmark perturbation tests

This experiment is carried out with consistency dataset and it shows the sensitivity of the overall registration to each anatomical landmark. Each landmark's X, Y, and Z coordinates are perturbed with -10 mm to $+10mm$ and anatomical landmark based registration without surface refinement is performed with the perturbed landmark. The graphs in Figures 4.1 to 4.5 are formed such that x-axis is perturbation amount and y-axis is the registration error. The Whisker-box plots show the mean and standard deviation of the registration error for the same (mm) amount of perturbation in different directions. The results indicate that the most sensitive landmarks are eye balls, and the less sensitive landmarks are the nose and CoS. These results also emphasize that landmark based registration error should be refined. Therefore, our head surface based registration stage after the landmark based registration is a

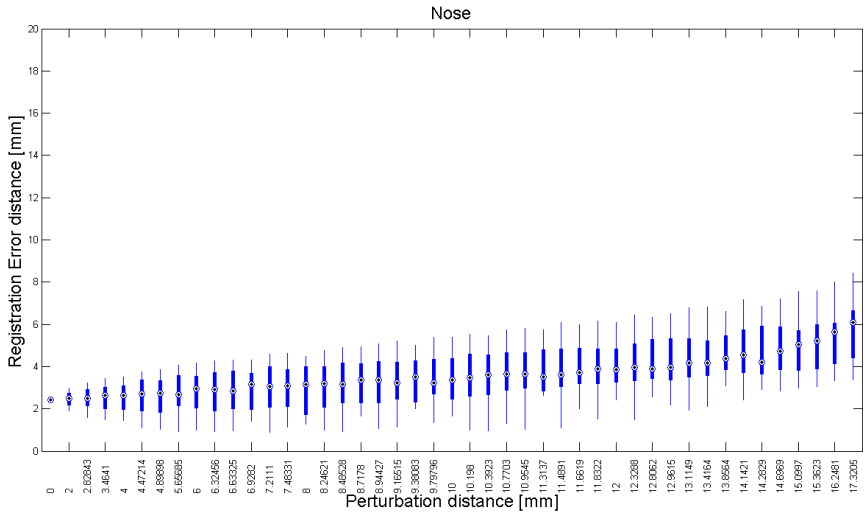

Figure 4.1: Perturbation of nose landmark.

valid refinement approach to correct possible errors in landmark extraction.

4.3 Validation Studies on T1-MRI

4.3.1 Validation Studies on a Dataset with Fiducial Landmarks

For a validation study on a real MRI data, fish oil tablets are used as fiducial landmarks, and 6 tablets are positioned with an unbiased sampling over the surface of the head of a patient. Two CE-T1 MRI scans are performed: the first scan in a regular patient position, and the second scan performed after the patient head is gently tilted about the axial axis. For both scans, fiducial landmarks are segmented and a rigid transformation matrix is calculated using the method described in Section 3.2.1. These parameters are used as the "ground truth" transformation parameters in this experiment. Fiducial landmarks are then removed from both of the volumes, and anatomical landmarks are automatically extracted, and registration is performed as described in Section 3.2. The two fiducially marked volumes are also aligned using the mutual information based registration algorithm, which we implemented in matlab. Differences between the estimated transformation parameters and the "ground truth" parameters are reported in Table 4.2. The parameters

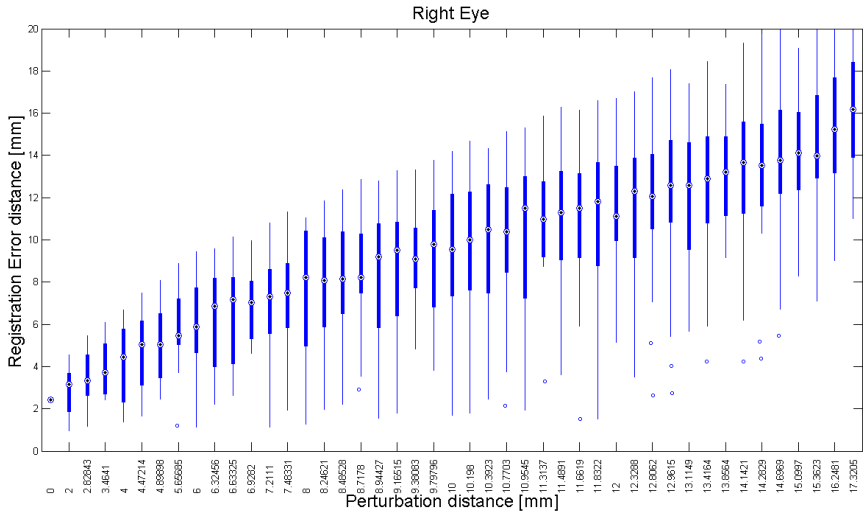

Figure 4.2: Perturbation of right eye landmark.

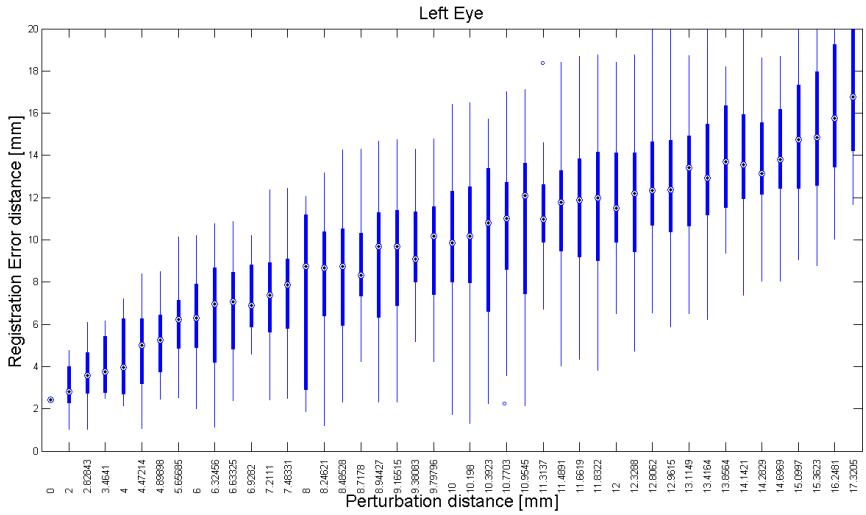

Figure 4.3: Perturbation of left eye landmark.

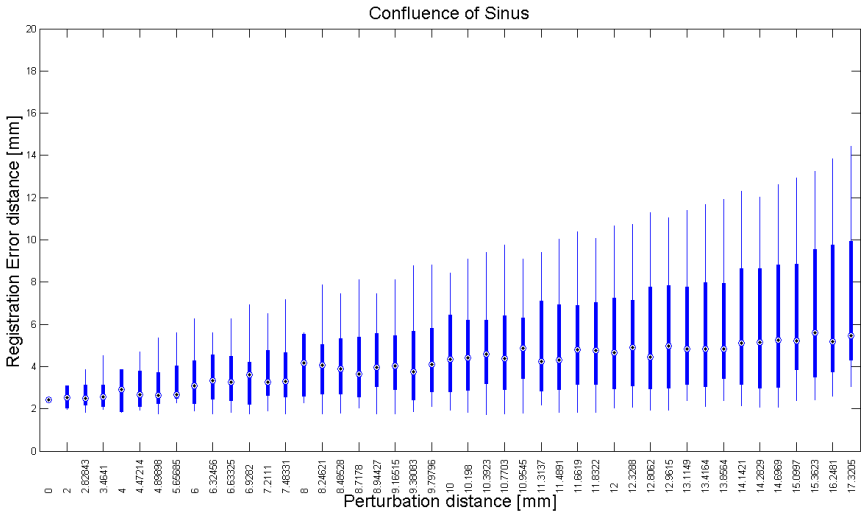

Figure 4.4: Perturbation of CoS landmark.

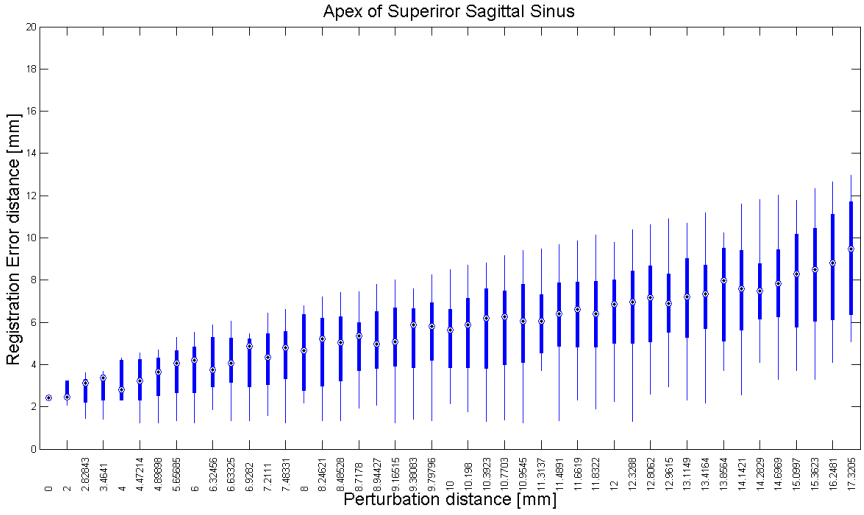

Figure 4.5: Perturbation of SSS landmark.

Table 4.2: Transformation error measures for fiducial landmark data. Rotation error is reported in the sense of Frobenius norm between the two rotation matrices.

Registration Method	Rotation Error	Translation Error (mm)
Landmark based	0.013	0.54
Landmark based with surface refinement	0.016	0.45
Mutual Information based	0.496	8.18

estimated by the proposed registration method were closer to the "ground truth" parameters than those of the mutual information based method for the fiducially marked volumes.

4.3.2 Studies on Follow-up CE-T1 MRI

In order to show the effect of the surface registration step (Section 3.2.2) in our algorithm, an intensity based measure, a normalized sum of squared intensity differences (SSID) is utilized:

$$SSID = \int_{\Omega} \frac{[I(\boldsymbol{X}_f) - I'(\boldsymbol{T}(\boldsymbol{X}_m))]^2}{[I(\boldsymbol{X}_f) + I'(\boldsymbol{T}(\boldsymbol{X}_m))]^2} \, d\Omega \tag{4.1}$$

where I is the fixed intensity image and I' is the registered intensity image. Follow-up MRI scans were registered to their baseline scans and the SSID results are presented in Table 2. The results in table are obtained from 4 different region of interests with size of 30x30x5 mm which are carefully chosen apart from brain tumor especially on cerebrospinal fluid edges. For most of the registration experiments intensity based method is gives slightly smaller SSID error rates. We observed that the change of tumor tissue amount in follow-up MRI causes a significant change in intensity distribution and we showed that for certain cases (Case 3: Figure 4.6) intensity based method might be problematic.

Table 4.3: Transformation error measures of consistency dataset

	SSID of Our Landmark Based Reg.	SSID of Itk Mean Squares Error Based Reg.
Case 1	0.022380 ∓ 0.013079	0.022385 ∓ 0.016152
Case 2	0.008561 ∓ 0.006431	0.007971 ∓ 0.006405
Case 3	0.015537 ∓ 0.011956	0.018244 ∓ 0.015934
Case 4	0.012373 ∓ 0.005624	0.010563 ∓ 0.003264
Case 5	0.015914 ∓ 0.011605	0.012994 ∓ 0.009819
Case 6	0.019233 ∓ 0.016307	0.019518 ∓ 0.015773
Case 7	0.037024 ∓ 0.038771	0.035345 ∓ 0.038085

4.3.3 Validation Studies with manual expert guided registration

For comparison of our automatic landmark extraction to an expert's manual landmark extraction, one radiologist in our team manually marked 6 landmarks, which are not necessarily the computationally extracted landmarks (since for instance it is not possible to visually mark the 3D centroid of eyeballs), in two baseline and corresponding follow-up CE-T1 MRI volumes. Registration is performed using these expert guided manual anatomical landmarks, and also using the proposed method (both with and without surface refinement step). Qualitative comparison of manual expert guided registration results indicate that manual landmark based registration is not appropriate ground truth for comparison.

4.3.4 Qualitative Results

We show sample image registration results for qualitative evaluation of the proposed method. Figure 4.6 and Fig.4.8 show image slices from two different patients having tumors appearing in various locations of the brain. The follow-up scan, which was performed several months later, was aligned with the baseline scan using the proposed rigid registration method. In Figure 4.7 and 4.9 we overlayed the registered

follow-up volume to reference baseline volume in a checkerboard pattern, that is, green patches correspond to baseline image, and red patches correspond to follow-up image regions. As can be observed in the checker board view, the proposed method successfully registered the two CE-T1 MRI volumes, which are routinely used in monitoring tumor progress and response to therapy. In both cases, after treatment, the tumors regressed significantly, with reduced margins as observed in the follow-ups.

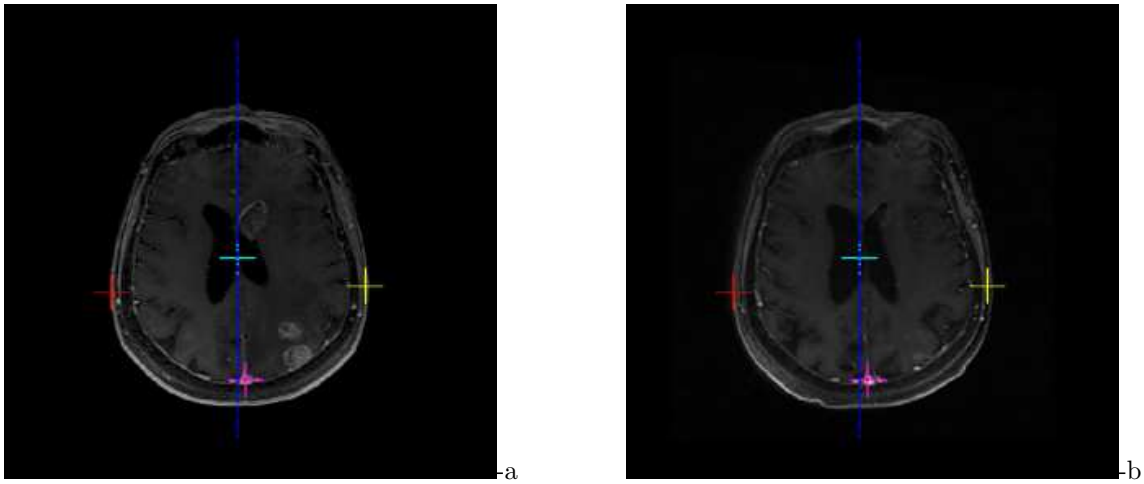

Figure 4.6: Qualitative evaluation of a sample case with 3 months follow-up volume registration results: a)Baseline slice, b)Registered Follow-up slice

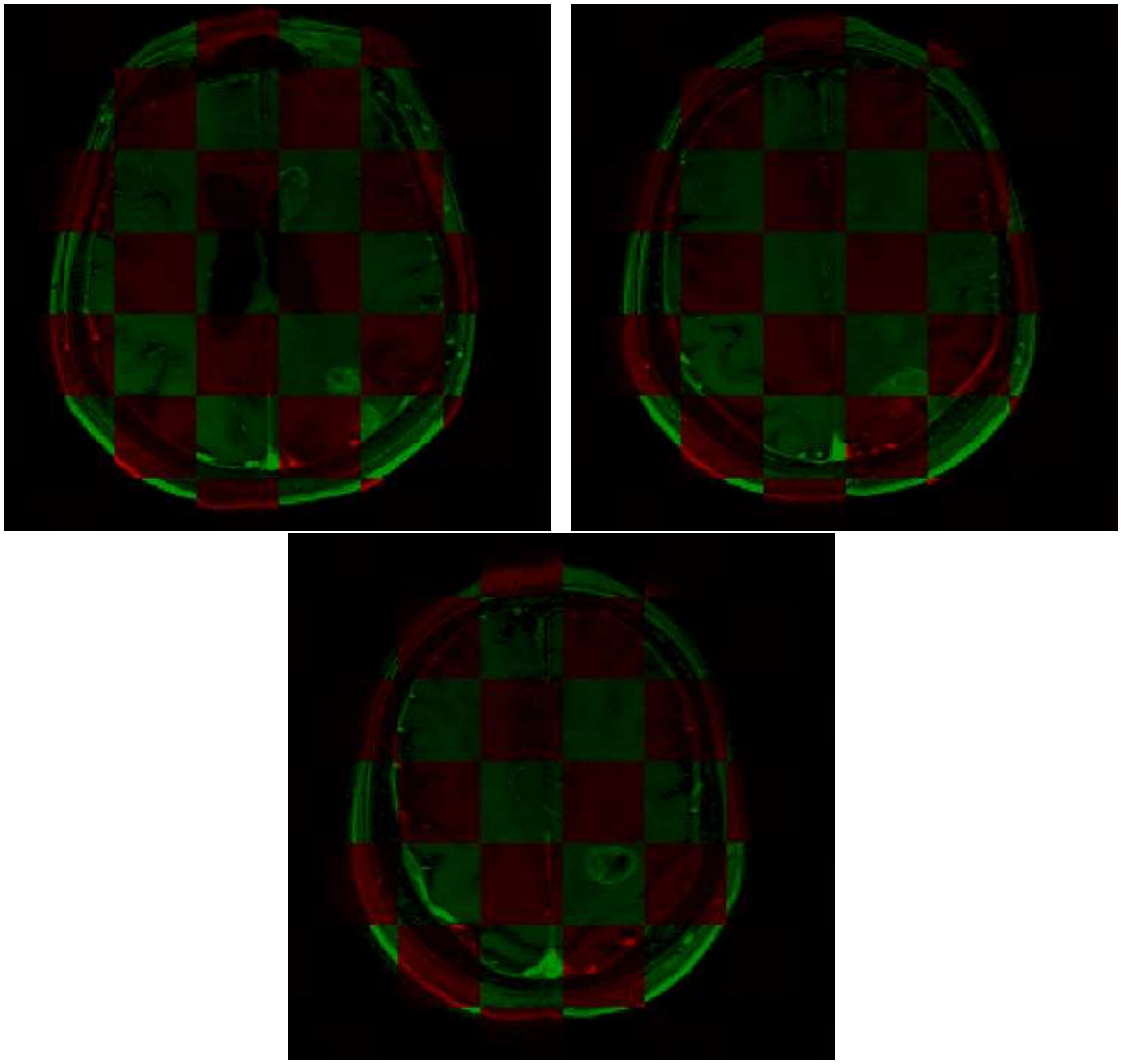

Figure 4.7: Checker board view with baseline image slices (green patches) and registered follow-up slices (red patches).

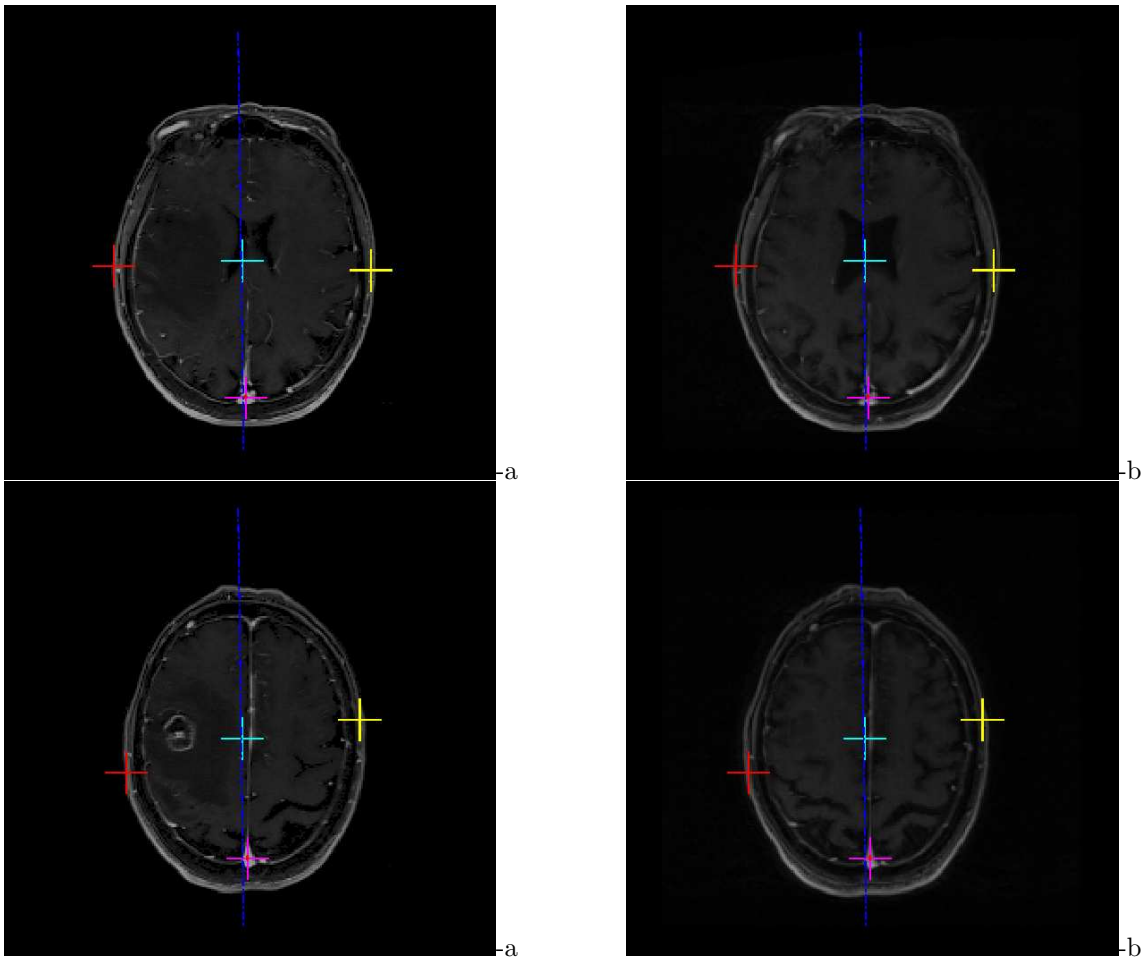

Figure 4.8: Qualitative evaluation of a sample case with 6 months follow-up volume registration results: a)Baseline slice, b)Registered Follow-up slice

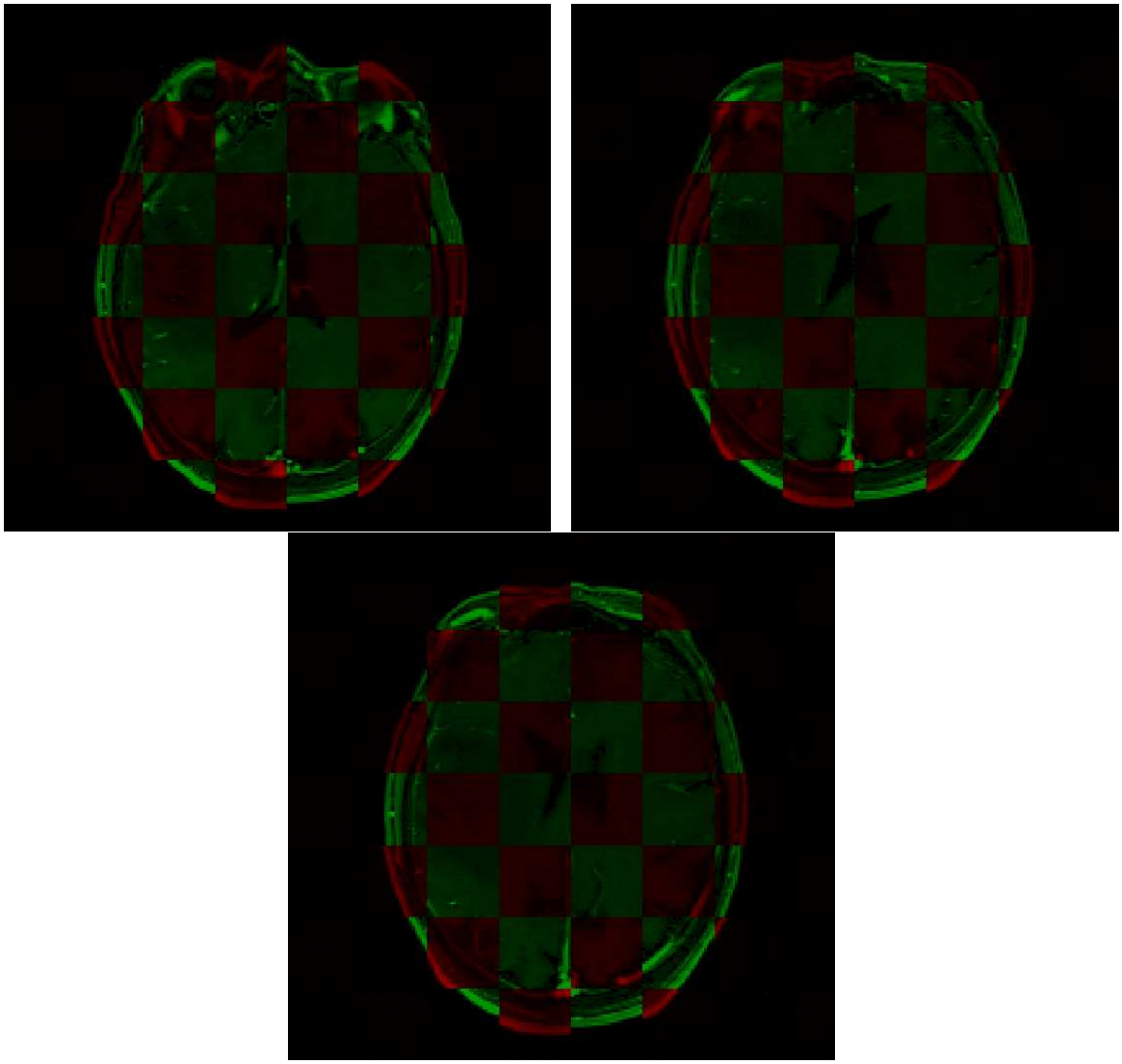

Figure 4.9: Checker board view with baseline image slices (green patches) and registered follow-up slices (red patches).

Chapter 5

Conclusions and Future Work

In this thesis, we presented a new rigid registration method, which is based on original anatomical features extracted from brain CE-T1 MRI volumes. A landmark-based registration based on the new anatomical landmarks was refined with a head surface-based registration, which provided an improved alignment of the head surfaces. One main application is the registration of follow-up MRI volumes in brain tumor patients, where the image intensity characteristics will vary due to tumor growth and possible different contrast characteristics depending on the scan acquisition time of the CE-T1 MRI scans. The presented landmark-based registration method, is relatively more robust against such changes, as it is not directly based on an intensity-based optimization procedure, and is only prone to errors at the anatomic landmark extraction stage. Various validation studies demonstrated the performance of the proposed method to be as accurate as the state-of-the-art (e.g. Itk Mean Squares and Normalized Correlation based registration), and more efficient in terms of computation times of the algorithm, and it successfully registers CE-T1 MRI volumes.

Future directions of our work includes:

- Improvement of the robustness of feature extraction,
- Implementation of the algorithm in a multi-resolution framework,
- Definition and extraction of new potential anatomical landmarks,
- Use of the proposed method in quantification of tumor change in serial MRI sequences.

Appendix A

Region based sphere evolutions

A.1 Eulerian Derivative of Equation 3.2

Eulerian Derivative of Equation 3.2 in the direction of $\boldsymbol{V}$ (Sokolowski and Zolesio (1992)):

$$E'(\lambda) = \int \frac{\partial f}{\partial \lambda}(\boldsymbol{X}, \lambda)dx - \oint_{\boldsymbol{C}_{in}} f(v \cdot \mathbf{N})d\lambda \tag{A.1.1}$$

where first term is variation of functional $f(x, y, z) = (I(x, y, z) - \mu_{in})^2 - (I(x, y, z) - \mu_{out})^2$, μ_{in} and μ_{out} are mean intensity of inside and outside of the sphere. This formulation assumes that $f(x, y, z)$ does not vary during evolutions. Therefore, the first term vanishes. Second term represents the motion of the sphere with respect to its parameters (λ^j).

A.2 Open form of Equation 3.4

$\frac{\partial \boldsymbol{X}}{\partial \lambda^j}$ can be expressed in terms of all sphere parameters ($\lambda^j = (r, a, b, c)$) as the following:

$$\frac{\partial \boldsymbol{X}}{\partial r} = \begin{pmatrix} cos(s)\ sin(p) \\ sin(s)\ sin(p) \\ cos(p) \end{pmatrix} \tag{A.2.2}$$

$$\frac{\partial \boldsymbol{X}}{\partial a} = \begin{pmatrix} 1 \\ 0 \\ 0 \end{pmatrix} \tag{A.2.3}$$

$$\frac{\partial \boldsymbol{X}}{\partial b} = \begin{pmatrix} 0 \\ 1 \\ 0 \end{pmatrix} \tag{A.2.4}$$

$$\frac{\partial \boldsymbol{X}}{\partial c} = \begin{pmatrix} 0 \\ 0 \\ 1 \end{pmatrix} \tag{A.2.5}$$

Bibliography

[1] Modersitzki, J.: Numerical methods for image registration. Oxford Univ Press, (2004)

[2] Zitova, B., Flusser, J.: Image registration methods: a survey. Image and Vision Computing 21, 977–1000 (2003)

[3] Fischer, B., Modersitzki, J.: Ill-posed medicine–an introduction to image registration. Inverse Problems 24, 1–16 (2008)

[4] Maintz, J., Viergever, M.: A survey of medical image registration. Medical Image Analysis 2, 1–36 (1998)

[5] Angelini, E., Clatz, O., Mandonnet, E., Konukoglu, E., Capelle, L., Duffau, H,: Glioma Dynamics and Computational Models: A Review of Segmentation, Registration, and In Silico Growth Algorithms and their Clinical Applications. Current Medical Imaging Reviews 3, 262–176 (2007)

[6] Patriarche, J., Erickson, B.: A Review of the Automated Detection of Change in Serial Imaging Studies of the Brain. J Digit Imaging 17, 158–174 (2004)

[7] Canny, J.: A Computational Approach To Edge Detection, IEEE Trans. Pattern Analysis and Machine Intelligence, 8(6):679-714, (1986)

[8] Ettinger, G. J., Grimson, W. E. L., Lozano-Perez, T., Wells III, W. M., White, S. J., and Kikinis, R.: Automatic registration for multiple sclerosis change detection. In IEEE workshop on biomedical image analysis, Los Alamitos, CA. 297–306 (1994)

[9] Chui, H., Win, L., Schultz, R., Duncan, J.S., Rangarajan, A.: A unified non-rigid feature registration method for brain mapping. Med Image Anal. 7(2), 113–130 (2003)

[10] Davatzikos, C., Prince, J. L.: Brain image registration based on curve mapping. In IEEE workshop on biomedical image analysis, Los Alamitos, CA. 245–254 (1994)

[11] Davatzikos, C., Prince, J. L., and Bryan, R. N.: Image registration based on boundary mapping. IEEE Transactions on medical imaging, 15(1), 112–115 (1996)

[12] Klein, A., Ghosh, S.S, Avants, B., Yeo, B.T.T., Fischl, B., Ardekani, B., James C. Gee, J.C., Mann, J.J., Parsey, R.V.: Evaluation of volume-based and surface-based brain image registration methods, NeuroImage, 51(1), 214–220 (2010)

[13] Douglas, N.G., Bruce, F.: Accurate and robust brain image alignment using boundary-based registration. NeuroImage, 48(1), 63–72 (2009)

[14] Christensen, G.E.: Inverse consistent registration with object boundary constraints. IEEE International Symposium on Biomedical Imaging, 1, 591–594 (2004)

[15] Talairach, J., Tournoux, P.: Co-planar stereotaxic Atlas of the Human Brain. Thieme Medical Publishers, (1988)

[16] Verard, L., Allain, P., Travere, J.M, Baron, J.C, Bloyet, D.: Fully Automatic Identification of AC and PC Landmarks on Brain MRI Using Scene Analysis IEEE transactions on Medical Imaging 16(5), 610–616 (1997)

[17] Maheswaran, S., Barjat, H., Bate, S.T., Aljabar, P., Hill, D.L.G., Tilling, L., Upton, N., James, M.J., Hajnal, J.V., Rueckert, D.: Analysis of serial magnetic resonance images of mouse brains using image registration, NeuroImage, 44(3), 692–700 (2009)

[18] Rohr, K., Stiehl, H., Sprengel, R., Buzug, T., Weese, J., Kuhn, M.: Landmark-based elastic registration using approximating thin-plate splines. IEEE Trans. Med. Img. 20(6), 526–534 (2001)

[19] Thirion, J.P.: New feature points based on geometric invariants for 3d image registration. Int. J. of Computer Vision 18(2), 121–137 (1996)

[20] Viola, P.A., Wells, W.M.: Alignment by maximization of mutual information. International Journal of Computer Vision 24(2), 137–154 (1997)

[21] Penney, G.P., Weese, J., Little, J.A., Desmedt, P., Hill, D.L.G., Hawkes, D.J.: A comparison of similarity measures for use in 2-D-3-D medical image registration. IEEE Trans. on Med. Imaging 17, 586–594 (1998)

[22] Pluim, J., Maintz, J., Viergever, M.: Image registration by maximization of combined mutual information and gradient information. IEEE Trans. on Med. Imaging 19(8), 809–814 (2000)

[23] Fitzpatrick, J.M., West, J.B., Maurer, C.R.J.: Predicting error in rigid-body point-based registration. IEEE Trans. Med. Imaging 17, 694–702 (1998)

[24] Jenkinson, M., Smith, S.: A global optimisation method for robust affine registration of brain images. Med Image Anal. 5(2), 143–56 (2001)

[25] Gonzalez, Rafael C. and Woods, Richard E. Digital Image Processing. Addison-Wesley Longman Publishing Co., Inc. (2001)

[26] Golub, G.H., Van Loan, C.F.: Matrix Computations. JHU Press. (1996)

[27] Qt by Nokia, http://qt.nokia.com (2010)

[28] Ibanez, Schroeder, Ng, Cates. The ITK Software Guide, Second Edition Kitware Inc. (2005) ISBN: 1-930934-15-7

[29] Will Schroeder, Ken Martin, and Bill Lorensen. The Visualization Toolkit, Third Edition. Kitware Inc. (2005)

[30] R.M. Murray, and Z. Li and S. Sastry: A Mathematical Introduction to Robotic Manipulation. CRC Press. (1994)

[31] Zouhar, A., Fang, T., Unal, G., Slabaugh, G., Xie, H., McBagonluri, F.: Anatomically-Aware, Automatic, and Fast Registration of 3D Ear Impression Models. Proc. of the Third International Symposium on 3D Data Processing, Visualization, and Transmission. (2006)

[32] Demir, A., Unal, G., Karaman, K.: Automatic registration of follow-up brain MRI scans, Biyomut 2009, 1, 1–4 (2009)

[33] Demir, A., Unal, G., Karaman, K.: Anatomical landmark based registration of contrast enhanced T1-weighted MR Images, International Workshop on Biomedical Image Registration, to appear in Springer's Lecture Notes in Computer Science, (2010)